University of Strathclyde

Department of Naval Architecture, Ocean and Marine Engineering

Peridynamic Analysis of Fatigue Crack Growth in Fillet Welded Joints

By

KyuTack Hong

A thesis Submitted in fulfilment of the requirements for the degree of

Master of Philosophy

Glasgow, U.K.

August 2018

DECLARATION

This thesis is the result of the author's original research. It has been composed by the author and has not been previously submitted for examination which has led to the award of a degree

The copyright of this thesis belongs to the author under the terms of the United Kingdom Copyright Acts as qualified by University of Strathclyde Regulation 3.50. Due acknowledgement must always be made of the use of any material contained in, or derived from, his thesis.

Signed:

Date:

ABSTRACT

Fatigue assessment is one of the significant factors to be considered for a design life of structure and estimation of structural reliability during operation. Especially, for welded structures, various welding effects, such as stress concentration, residual stresses, weld geometry and weld quality, make the structure more vulnerable to fatigue failures. This requires more effective approaches for estimating fatigue performances of welded structures.

Existing classical methods to predict the crack propagation under cyclic loadings have some difficulties in treating complicated patterns of crack growth. A peridynamic theory, however, has powerful advantage on discontinuities. A peridynamic fatigue model, which is a bond damage model of remaining life, is used to demonstrate two phases of fatigue failure, crack nucleation and crack growth. Two types of numerical tests are conducted to validate the peridynamic fatigue model. One is tensile test for the phase of crack nucleation and the other is compact tension test for the phase of crack growth. All results from numerical tests are compared with experimental test data to validate the peridynamic fatigue model.

After validation of peridynamic fatigue model, numerical tests with peridynamic fatigue model are performed to investigate a weld effect of the length of unwelded zone on the fatigue performance of load-carrying fillet welded joint. Numerical results of fatigue performance and path of fatigue crack growth are compared with existing experimental data.

In this thesis, the peridynamic fatigue model is validated by two different fatigue tests which are uniaxial tension-compression tests for the crack nucleation and ASTM E647 standard compact tests for the crack growth. After validation, the fatigue performance of the fillet welded joint is estimated with respect to the length of unwelded zone by simulating the fatigue crack growth under cyclic load conditions with the peridynamic fatigue model.

ACKNOWLEDGEMENTS

CONTENTS

LIST OF TABLES

LIST OF FIGURES

NOMENCLATURE

N_f	Number of cycles to failure
C_f	Fatigue constants in Stress-Life curve
m_f	Fatigue constants in Stress-Life curve
ΔS	Stress range
D	Fatigue damage
T	Number of different stress range
n_i	Number of cycles of the ith stress range
N_i	Number of cycles to failure of the ith stress range
σ	Fatigue constants in Stress-Life curve
a	Crack length
K_c	Fracture toughness
ΔK_{th}	Threshold of stress intensity range
N	Number of cycles
ΔK	Stress intensity range
C	Fatigue crack growth constants of Paris law
M	Fatigue crack growth constants of Paris law
K_c	Critical stress intensity factor
$\mathbf{x}_{(k)}$	Position vector at a material point "k"
$\mathbf{u}_{(k)}$	Displacement vector at a material point "k"
H_k	Horizon of a material point "k"

ρ	Mass density field
$\mathbf{f}$	Pairwise force function
$\mathbf{b}$	Body force density field
t	Time
$\mathbf{\xi}_{(k)(j)}$	Relative position between a material point "k" and a material point "j"
$\mathbf{\eta}_{(k)(j)}$	Relative displacement between a material point "k" and a material point "j"
c	Bond constant
$s_{(k)(j)}$	Bond stretch between a material point "k" and a material point "j"
μ	History-dependent scalar-valued function
s_0	Critical bond stretch
G_0	Energy release rate
K_B	Bulk modulus
δ	Horizon
φ	Local damage
$\rho_{(k)}$	Mass density of the material point "k"
n	n^{th} time step number
Q	Number of material points within the horizon of the material point "k"
$\mathbf{u}_{(k)}^{n}$	displacement of the material point "k" at the nth time step number
$V_{(k)}$	volume of the material point "k"
$\mathbf{b}_{(k)}^{n}$	body force density of the material point "k" at the nth time step number

Δt	Time step size
$\lambda_{(k)(j)}$	Remaining life of a bond between a material point "k" and a material point "j"
A	Peridynamic fatigue parameter
m	Peridynamic fatigue parameter
$\varepsilon_{(k)(j)}$	Cyclic bond strain of a bond between a material point "k" and a material point "j"
s^+	Maximum bond stretches in a cycle
s^-	Minimum bond stretches in a cycle
R	Load ratio
A_1	Peridynamic fatigue parameter for the phase of crack nucleation
m_1	Peridynamic fatigue parameter for the phase of crack nucleation
A_2	Peridynamic fatigue parameter for the phase of crack growth
m_2	Peridynamic fatigue parameter for the phase of crack growth
N_1	Number of cycles to the first bond breakage
ε_1	Cyclic bond strain of bond which will break first
$\bar{\varepsilon}$	Cyclic bond strain function of position relative to the crack tip
$\bar{\lambda}$	Remaining life function of position relative to the crack tip
z	Position coordinate based on the crack tip along the mode-1 crack axis
x	spatial coordinate along the mode-1 crack axis
f	Function to represent the distribution around a crack tip

$\mathbf{K}_{ij}$	Stiffness matrix of the equation system
Q_i	Number of family of ith material point
N_t	Total number of material points
$\mathbf{C}$	Second-order material's micromodulus tensor
$\mathbf{M}$	Unit vector of bond direction
θ	Angle of bond from the x-axis in the reference configuration
$\theta_{(k)(j)}$	Angle of bond between two material points "k" and "j" from the x-axis in the reference configuration
$\mathbf{K}_{\mathrm{G}}$	Global stiffness matrix
$\mathbf{U}_{\mathrm{G}}$	Global displacement matrix
$\mathbf{F}_{\mathrm{G}}$	Global body force vector
ε_0	Fatigue limit
C'	Fatigue crack growth constants of modified Paris law
M'	Fatigue crack growth constants of modified Paris law
γ	Fatigue crack growth constants of modified Paris law
K_{max}	Maximum stress intensity factor in a cycle
ΔK^+	Positive part of the range of the stress intensity factor in a cycle
$\varepsilon_{(k)(j)_{max}}$	Maximum cyclic bond strain between material points "k" and "j"
$\Delta \varepsilon_{(k)(j)}^{+}$	positive part of the range of cyclic bond strain between material points "k" and "j"
K	Stress intensity factor
P	Applied force
B	Thickness of the compact specimen

W	Distance between the right edge of the specimen and the vertical line of the applied force
$c_{(k)(j)}$	Bond constant between material points "k" and "j"
l_1	Segment of the distance between material points in material 1
l_2	Segment of the distance between material points in material 2
c_1	Bond constant in material 1
c_2	Bond constant in material 2

1) INTRODUCTION

1.1 Overview

In the recent years, large ships and offshore structures are produced by joining processes and the most commonly used method for joining processes is welding. In welded structures, however, there are some effects to make their welding zone vulnerable in fatigue failures, such as residual stresses, weld geometry and weld quality [1-3]. Particularly, many welded joints have inherently poor fatigue performance, since the crack growth can easily initiate at embedded cracks where there are high stress concentrations. The fatigue performance of many welded joints is typically estimated based on empirical data obtained from fatigue tests for different weld details. It requires much effort both in time and cost to establish the fatigue performance of many types of welded joints.

Instead of experimental fatigue tests, computational approaches are available to save time and cost. A finite element method is one of the major computational methods to estimate the fatigue performance of structures. In finite element method, all calculations are based on partial differential equations of classical continuum mechanics, which means there is inherent limitation of singularities when treating discontinuities, such as a crack. To overcome this limitation, a cohesive model is introduced for tracking of dynamically growing cracks [4-5]. However, it requires a priori knowledge of the path of crack propagation and cracks in cohesive model are mesh-dependent, which means crack propagations occur only along element boundaries. For the problem of mesh-dependency in the cohesive model, an extended finite element method is introduced as an alternative to the cohesive model [6-8]. The extended finite element method can treat cracks independent of mesh, but there are still difficulties to determine the direction of crack propagation in three-dimensional models and it requires additional failure criteria.

A meshless method of an alternative to methods based on the classic continuum mechanics, peridynamic theory, is introduced by Silling [9]. In peridynamics, it is assumed that particles in a body interact with all particles within the body, as in molecular dynamics. The peridynamic theory can treat discontinuities and material

failures without additional necessaries for dictating the crack growth. Peridynamic equations do not involve partial derivatives, instead it involves integral equations. Therefore, it is possible to predict accurately crack initiation and crack propagation without any special techniques, and also it can predict complex patterns of crack in structures [10-12].

1.2 Motivation

The fatigue performance is generally estimated from fatigue tests, and results are expressed as Stress-Life curves. Particularly, since welded structures have inherently poor fatigue performance, it is necessary to consider carefully fatigue performances of many types of welded joints in structures. However, there are many factors effecting on the fatigue performance. Even small factors can effect on the fatigue performance significantly. Considering all these factors fatigue tests are costly and time-consuming. Alternatively, computational approaches, such as a finite element method, are available, but there are still difficulties to predict the accurate crack growth and complex crack growth patterns in structures. Consequently, it is necessary to develop a new computational approach for simulating fatigue failures and estimating the fatigue performance of various welded structures.

1.3 Objectives

Objectives of this study are to suggest and demonstrate a new computational approach with the peridynamic fatigue model to estimate the fatigue performance of welded joints. This study has two main objectives:

- To validate the peridynamic fatigue model proposed by Silling and Askari [13] in each phase of fatigue failure including the crack nucleation and crack growth.

- To estimate the fatigue performance of fillet welded joints by predicting the fatigue crack growth in fillet welded joints.

In this study, a computational approach is developed by using the peridynamic fatigue model proposed by Silling and Askari [13]. Numerical results are compared with existing experimental results. Finally, the effect of unwelded zone on the fillet welded joint is investigated by simulating the fatigue crack growth in the fillet welded joints.

2) LITERATURE REVIEW

2.1 Review of fatigue analysis

Fatigue is a process of structural damage occurring in a material by cyclic loadings, which can develop cracks and complete fracture in the material after sufficient number of cycles. There are generally three phases of fatigue failure: crack initiation, crack growth and final fracture.

2.1.1 Stress-Life curve assessment

At the design stage, for structures without flaws, Stress-Life curves are typically used to predict the design life of structures. The Stress-Life curve is an empirical data obtained from fatigue tests of large number of specimens. Typical examples of Stress-Life curves are represented in Fig. 2.1, which show stress range versus number of cycles to failure. The general shape of Stress-Life curve is expressed as

$$N_f \Delta S^{m_f} = C_f \qquad (2.1a)$$
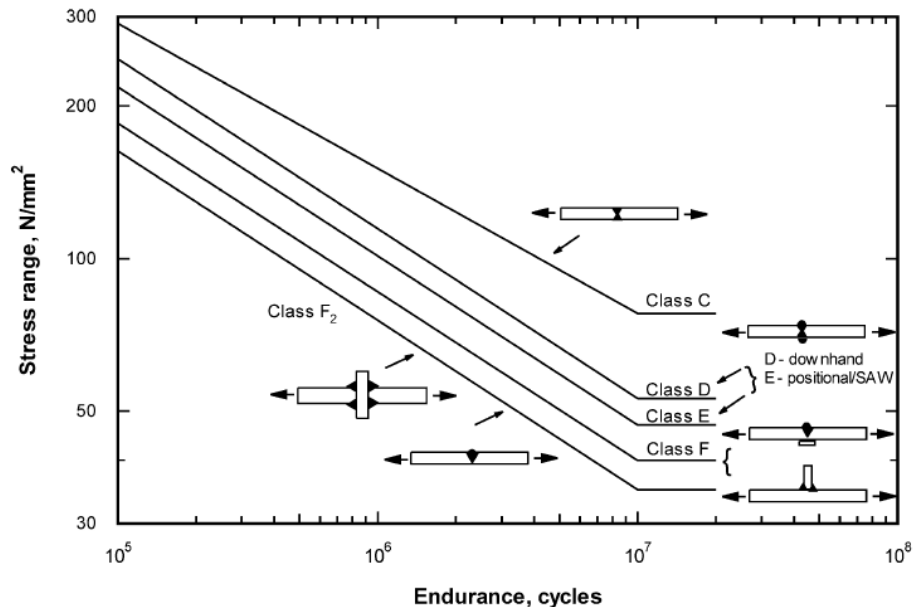
Figure 2.1. Stress-Life curves for fillet welds [14]

and

$$logN_f = logC_f - m_f log\Delta S \qquad (2.1b)$$

where N_f is the number of cycles to failure, ΔS is the stress range, C_f and m_f are constants.

To establish the required fatigue life, it is necessary to estimate the resulting stress history. A general method to count the cycles of stress history is rainflow counting method, which converts the stress history into number of cycles with respect to the stress range [15]. After counting, the fatigue damage is calculated by using Miner's rule which is a cumulative damage model. The Miner's rule is described as [15]

$$D = \sum_{i=1}^{T} \frac{n_i}{N_i} \qquad (2.2)$$

where D is the fatigue damage, T is the number of different stress range, n_i is the number of cycles of the ith stress range, and N_i is the number of cycles to failure of the ith stress range. n_i is obtained from the stress history and N_i is obtained from the Stress-Life curve. When the fatigue damage D becomes 1, the fatigue failure occurs.

2.1.2 Fatigue crack assessment

Strain-life curves are typically used in safe-life design, which establish a finite fatigue life for each design component. For example, if a structure with multiple components is subjected to loading and if one of the components fails, the whole system may not fail. Similarly, the Strain-Life curve can provide information to predict the crack initiation at a specific point, not for failure of the whole system. Once a crack is present in a material, the Strain-Life curve approach is not valid. Instead, the fracture mechanics is used for fatigue assessment of the material with a pre-existing crack.

In the fracture mechanics, for a material with cracks under a static or monotonic loading, the stresses near the crack tip are proportional to the stress intensity factor [16]. The stress intensity factor K is given by

$$K = f\left(\sigma, \sqrt{a}\right) \tag{2.3}$$

where σ is the stress applied to the material, and a is the crack length. The material can withstand a stress field at a crack tip below a critical value of stress intensity factor K_c which is a fracture toughness derived from fracture tests.

To predict the fatigue crack growth in structures, the fatigue crack growth rate of many types of materials has been investigated both theoretically and experimentally. The results of tests are compiled into Paris curves, which are plots of crack growth rate versus stress intensity range. A typical example of Paris curve is represented in Fig. 2.2. The Paris curve is typically divided into three regions. In region 1, there is a threshold of stress intensity range ΔK_{th}. If the stress intensity range is not greater than this threshold, the crack will not propagate. In region 2, Paris [17] discovered that the instantaneous crack growth rate is linearly proportional to the stress intensity range in the logarithmic scale plot given in Figure 2.2. The relation between crack growth rate and stress intensity factor is provided as [17]

$$\frac{da}{dN} = C\Delta K^M \tag{2.4}$$

where a is the instantaneous crack length, N is the number of cycles, ΔK is the stress intensity range, C and M are the fatigue crack growth constants. In region 3, the crack growth is accelerated and when the stress intensity factor reaches the critical stress intensity factor K_c, the fracture of final failure will occur.
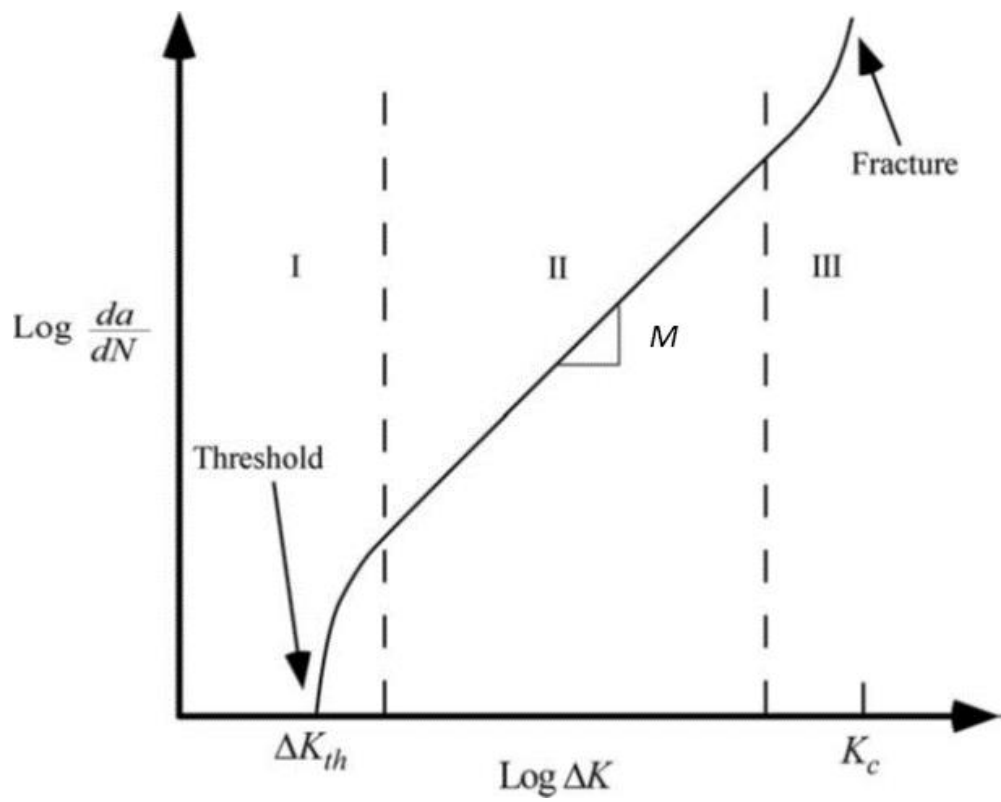
Figure 2.2. Typical Paris curve in materials [16]

2.2 Fatigue performance of welded joints

The fatigue performance of welded joints can be determined experimentally by considering various effects such as [15]

- Structural stress concentrations due to the weld geometry
- Weld imperfections
- Direction of loading
- Residual stresses
- Metallurgical conditions
- Welding process
- Post weld treatments

The effect of weld geometry has been investigated on various weld configurations such as weld flank angle, thickness, and weld toe radius. Ferreira and Branco [18] investigated the effect of geometric ratio (distance between weld toes over the material thickness) and the toe curvature on the fatigue performance of T-joints and cruciform joints. They predict fatigue performances based on linear elastic fracture mechanics (LEFM). The results showed that the fatigue performance of welded joints decreases as the geometric ratio increases and the increase in toe curvature led to higher fatigue performance. Nguyen and Wahab [19] evaluated the influence of the weld geometry on the fatigue performance of butt welded joints based on LEFM and finite element analysis. The results showed that the increase in weld toe radius led to improvement of fatigue strength of the butt welded joints. As the weld flank angle, thickness, edge preparation angle and tip radius of undercut at weld toe decrease, the fatigue strength of butt welded joints is improved. Lee and Chang [20] investigated the effect of weld geometry on the fatigue performance of cruciform fillet welded joints. Considering three welded geometry parameters such as weld flank angle, weld toe radius, and weld throat thickness, they assessed contributions of each parameter to their fatigue performance. The results showed that the fatigue strength was improved with increasing weld flank angle and weld toe radius, but the weld throat thickness has little contribution to fatigue performance.

There are several types of imperfection on welded joints. For example, misalignment can increase stresses in welded joints due to occurrence of secondary bending stresses. Weld imperfections, such as porosity, decrease the fatigue performance of welded joints. Wahab and Alam [21] investigated effects of various weld imperfections on the fatigue performance based on finite element method. The results showed that the crack and embedded porosity reduce significantly fatigue performances.

In general, residual stresses occur in welded joints as a result of thermal strains caused by heating and cooling cycles, which also affect the fatigue performance of welded structures. Ninh and Wahab [22] investigated the effect of residual stresses and weld geometry on the fatigue performance of butt welded joints. They made an analytical model based on LEFM, superposition principle and finite element method. The results of theoretical analysis showed that compressive residual stresses on weld toes improved the fatigue performance, while the increase in tensile residual stresses on weld toes deteriorated the fatigue performance. Teng and Chang [23] investigated an effect of residual stresses on the fatigue performance of butt welded joints based on finite element method. They simulated welding residual stresses at critical locations of butt welded joints and predicted the fatigue crack initiation based on the Strain-Life approach. The results showed that localized heating due to welding caused tensile residual stresses at weld toes and deteriorated the fatigue performance of butt welded joints.

The welding process has a significant effect on the fatigue life of the weld metal. This has a direct influence on the tensile properties and toughness of the fatigue crack growth. Magudeeswaran et al. [24] investigated the effect welding processes on fatigue crack growth behaviour of steel joints. Welding heat input and cooling rate play the decisive role in determining the microstructure of the weld metal in the welding process. They estimated the fatigue performance of joints fabricated by SMAW(Shielded Metal Arc Welding) and joints fabricated by FCAW(Flux-Cored Arc Welding), which the FCAW process is relatively higher heat input as compared with the SMAW process. The joints fabricated by SMAW process exhibited better fatigue performance compared to FCAW process. The results showed that the welding process with higher heat input condition decreased the fatigue performance of the welded joints.

The fatigue performance of the welded joints can be improved by post weld techniques. There are post-welded weld improvement methods: grinding, TIG(tungsten inert gas) dressing, hammer and needle peening [15]. The grinding and TIG dressing are methods to remove imperfection and create a smooth transition between weld for reducing the stress concentration. The hammer and needle peening deform the material plastically to introduce beneficial compressive residual stress at the weld toe.

2.3 Computational approaches for fatigue crack growth

One of the most popular methods for fatigue crack analysis is a finite element method which is based on the classical continuum mechanics for fatigue crack problems by introducing numerical techniques such as a cohesive element method, and an extended finite element method (XFEM).

First, cohesive laws have been introduced into finite element analysis as mixed boundary conditions by Hillerborg [25]. De-Andrés et al. [26] proposed a three-dimensional cohesive element model for an approach to fatigue life prediction, which is possible to track three-dimensional fatigue crack fronts and lead to the formation of free surfaces. They demonstrated simulations of fatigue crack growth in a three-dimensional model and compared the results with experimental test data. Nguyen et al. [27] developed a two-dimensional cohesive element model to predict fatigue life. They used the cohesive element model to predict fatigue crack growth. They also investigated effects of overloads on crack growth rates for long cracks.

Belytschko and Black [28] proposed a remeshing finite element method, which is called as XFEM, for modelling crack growth in materials. The XFEM has been developed to analyse the crack growth in a three-dimensional model which allows arbitrary crack growth [29-30]. Sukumar and Chopp [31] proposed a numerical technique for simulations of fatigue crack growth in a three-dimensional XFEM model. They demonstrated simulations of fatigue crack growth along planner surfaces and compared XFEM results with exact solutions. Their results showed good agreement with the theory.

Alternative to the cohesive element method and XFEM, in this study, peridynamics is introduced to solve the fatigue crack growth problems. The

peridynamic theory can treat discontinuities and material failures without additional necessaries for dictating the crack growth. Therefore, it is possible to predict fatigue crack growth without any special techniques.

3. PERIDYNAMIC THEORY

Peridynamic theory is an alternative theory of classical continuum mechanics to overcome limitations of discontinuity, which was proposed by Silling [32]. It is assumed that all points in a body are represented by material points which occupy a certain volume and interact with other material points within a finite distance called horizon δ. In peridynamic theory, there is physical interaction between the material points called bond which interacts with each other within the horizon as a force function. The equation of motion of any material can be expressed as [9]

$$\rho(\mathbf{x})\ddot{\mathbf{u}}(\mathbf{x}, t) = \int_{H_\mathbf{x}} \mathbf{f}(\mathbf{u}(\mathbf{x}', t) - \mathbf{u}(\mathbf{x}, t), \mathbf{x}' - \mathbf{x}) dV_{\mathbf{x}'} + \mathbf{b}(\mathbf{x}, t) \tag{3.1}$$

where $H_\mathbf{x}$ is the neighbourhood of material point $\mathbf{x}$ within the horizon δ, ρ is the mass density field, $\mathbf{x}$ is the position vector field, $\mathbf{u}$ is the displacement vector field, t is time, $\mathbf{f}$ is the pairwise force function which the material point $\mathbf{x}'$ exerts on the material point $\mathbf{x}$, and $\mathbf{b}$ is prescribed body force density field. The interaction of material points in peridynamic theory is shown in Fig. 3.1.

For a linear elastic material, the pairwise force function is given as [9]

$$\mathbf{f}(\mathbf{u}(\mathbf{x}', t) - \mathbf{u}(\mathbf{x}, t), \mathbf{x}' - \mathbf{x}) = \frac{\boldsymbol{\xi} + \boldsymbol{\eta}}{|\boldsymbol{\xi} + \boldsymbol{\eta}|} cs \tag{3.2a}$$
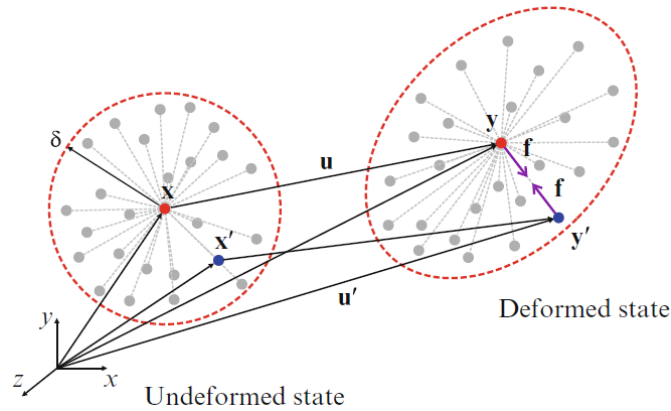
Figure 3.1. Deformation and interaction of material points $\boldsymbol{x}$ and $\boldsymbol{x}'$ [33]

$$\boldsymbol{\xi} = \mathbf{x}' - \mathbf{x} \qquad (3.2\text{b})$$

$$\boldsymbol{\eta} = \mathbf{u}(\mathbf{x}', t) - \mathbf{u}(\mathbf{x}, t) \qquad (3.2\text{c})$$

$$s = \frac{|\boldsymbol{\xi} + \boldsymbol{\eta}| - |\boldsymbol{\xi}|}{|\boldsymbol{\xi}|} \qquad (3.2\text{d})$$

where $\boldsymbol{\xi}$ is the relative position between material points $\mathbf{x}$ and $\mathbf{x}'$, $\boldsymbol{\eta}$ is the relative displacement between material points $\mathbf{x}$ and $\mathbf{x}'$, s is the bond stretch, and c the is bond constant which is determined by considering the strain energy density in the classical continuum mechanics for the same material and same deformation [9]. In three-dimensional linear elastic materials, the bond constant can be expressed as [9]

$$c = \frac{18K_B}{\pi \delta^4} \qquad (3.3)$$

where K_B is the bulk modulus and δ is the horizon.

When the bond stretch is greater than critical stretch, bond breakage occurs. The critical stretch s_0 is determined by considering the fracture energy, which is the energy that is required to create a unit crack surface [9]. For the linear elastic material, the critical stretch s_0 is expressed as [9]

$$s_0 = \sqrt{\frac{5G_0}{9K_B\delta}} \qquad (3.4)$$

where G_0 is the energy release rate, K_B is the bulk modulus, and δ is the horizon. To represent material failure, a history-dependent scalar-valued function μ is defined as

$$\mu = \begin{cases} 1 & if \; s(t', \boldsymbol{\xi}) < s_0 \quad for \; all \; 0 \le t' \le t \\ 0 & otherwise \end{cases} \qquad (3.5)$$

where s_0 is the critical bond stretch where failure occurs. A moment of bond failure is described in Fig. 3.2 [9].

Local damage at a material point is expressed as the ratio of the number of bond breakage to the total number of initial connected bonds of the material point. The local damage φ at the material point k can be quantified as below [9]

$$\varphi(\mathbf{x}, t) = 1 - \frac{\int_{H_{\mathbf{x}}} \mu(\mathbf{x}, t, \boldsymbol{\xi}) dV_{\mathbf{x}'}}{\int_{H_{\mathbf{x}}} dV_{\mathbf{x}'}} \qquad (3.6)$$

A range of local damage changes from 0 to 1. When the local damage is 0, all bonds are intact, while the local damage of 1 means that all bonds are broken. It can be used as an indicator of crack formation in the material.

To solve the peridynamic equation of motion of Eq. (3.1), it is necessary to be expressed in discretized form as

$$\rho_{(k)} \ddot{\mathbf{u}}_{(k)}^n = \sum_{j=1}^{Q} \mathbf{f}\left(\mathbf{u}_{(j)}^n - \mathbf{u}_{(k)}^n, \mathbf{x}_{(j)} - \mathbf{x}_{(k)}\right) V_{(j)} + \mathbf{b}_{(k)}^n \qquad (3.7)$$
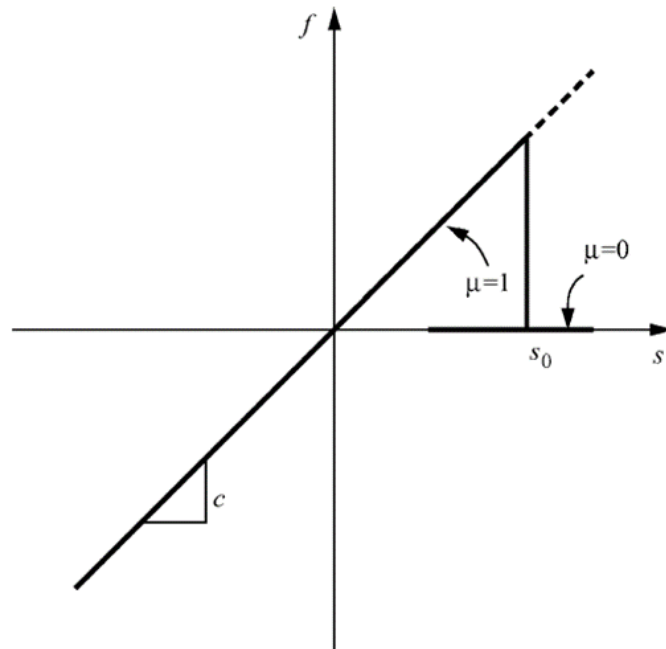
Figure 3.2. Pairwise force as a function of bond stretch and the value of μ with respect to s [9]

where $\rho_{(k)}$ is the mass density of the material point k, n is the nth time step number, Q is the number of material points within the horizon of the material point k, $\mathbf{u}_{(k)}^{n}$ is the displacement of the material point k at the nth time step, $V_{(j)}$ is the volume of the material point j, and $\mathbf{b}_{(k)}^{n}$ is the body force density of the material point k at the nth time step.

The velocity at the next time step can be calculated based on explicit forward difference formulations. The velocity at the $(n+1)^{th}$ time step is determined by the acceleration calculated from Eq. (3.7), and the velocity at the nth time step can be expressed as

$$\dot{\mathbf{u}}_{(k)}^{n+1} = \ddot{\mathbf{u}}_{(k)}^{n}\Delta t + \dot{\mathbf{u}}_{(k)}^{n} \tag{3.8}$$

where Δt is the time step size. The displacement at the $(n+1)^{th}$ time step is determined by the velocity calculated from Eq. (3.8), and can be found by using backward difference formulation as

$$\mathbf{u}_{(k)}^{n+1} = \dot{\mathbf{u}}_{(k)}^{n+1}\Delta t + \mathbf{u}_{(k)}^{n} \tag{3.9}$$

To obtain convergent results, it is necessary to consider a stability condition for the explicit time integration. The stability condition for the time step size Δt is derived based on von Neumann stability analysis as [9]

$$\Delta t < \sqrt{\frac{2\rho_{(k)}}{\sum_{j=1}^{Q} \frac{c}{\left|\mathbf{x}_{(j)} - \mathbf{x}_{(k)}\right|} V_{(j)}}} \tag{3.10}$$

4. PERIDYNAMIC FATIGUE MODEL

A first peridynamic fatigue model has been proposed by Oterkus, et al [34]. Their study represented the crack growth of a pre-existing crack by assuming a critical stretch which decreases with cyclic loading, but their fatigue model was only for phase of crack growth. To deal with all phases of fatigue failure, Silling and Askari [13] has proposed a single peridynamic fatigue model called the "remaining life" consumed by repeated loadings. The developed model can be applied for both phases of crack nucleation and crack growth by using different fatigue parameters in each phase of fatigue failure. This peridynamic fatigue model is bond-based peridynamic model for a linear elastic material.

4.1 Remaining life

In peridynamics, local damage in a material is quantified by the number of broken bonds. Bond breakage occurs when the bond stretch between two material points exceeds its critical value. By considering the fatigue behaviour of a material, a concept of remaining life has been introduced by Silling and Askari [13]. This peridynamic fatigue model assumed that the life of bond connected between two material points is consumed by cyclic loadings. The life reduction ratio of remaining life is determined by following relation [13]

$$\frac{d\lambda_{(k)(j)}}{dN} = -A\big(\varepsilon_{(k)(j)}\big)^m \tag{4.1a}$$

and

$$\lambda^0_{(k)(j)} = 1 \tag{4.1b}$$

where $\lambda_{(k)(j)}$ is the remaining life of bond between material points k and j, N is the number of cycles, A and m are peridynamic fatigue parameters, $\lambda^0_{(k)(j)}$ is the remaining life at the initial condition at 0th load cycle and $\varepsilon_{(k)(j)}$ is the cyclic bond

strain of the bond between material points k and j. The cyclic bond strain is defined as [13]

$$\varepsilon_{(k)(j)} = \left| s^+_{(k)(j)} - s^-_{(k)(j)} \right| \tag{4.2}$$

where $s^+_{(k)(j)}$ and $s^-_{(k)(j)}$ are the maximum and minimum bond stretches between material points k and j, respectively. They represent two extreme loading conditions in a cycle. For an elastic material, it is assumed that [13]

$$s^-_{(k)(j)} = R s^+_{(k)(j)} \tag{4.3}$$

where R is defined as the load ratio. Substituting Eq. (4.3) into Eq. (4.2) leads to

$$\varepsilon_{(k)(j)} = \left| s^+_{(k)(j)} - s^-_{(k)(j)} \right| = \left| (1-R) s^+_{(k)(j)} \right| \tag{4.4}$$

If a material is subjected to repeated loadings, it is assumed that the cyclic bond strain is independent of number of cycles N and peridynamic fatigue parameters A and m are independent of the position in the material [13].

Bonds in two different phases are represented in Fig. 4.1. Bonds near a crack tip within a boundary are involved in the crack growth phase, and the other bonds out of the boundary are involved in the crack nucleation phase. The boundary is defined as the horizon of material points on pre-existing crack tips [13].
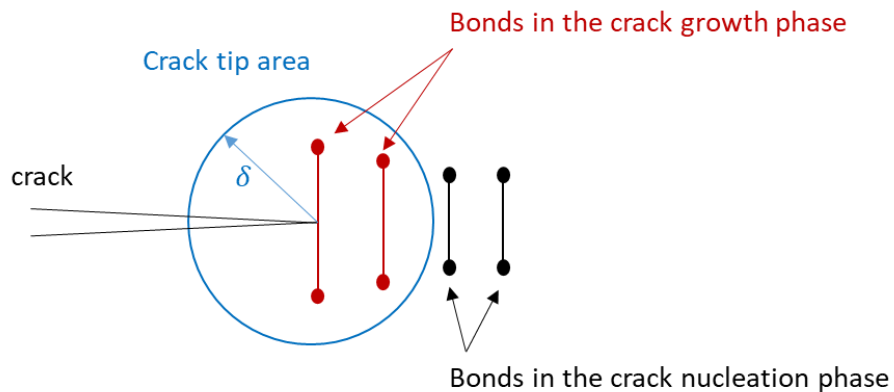
Figure 4.1 Bonds in two different phases of crack nucleation and crack growth

4.2 Crack nucleation

Remaining life of each bond in a material inherently has an initial value (Eq. (4.1b)) and is gradually consumed by cyclic loadings. When the remaining life reaches 0 or is less than 0, bond breakage occurs. Once the bond breaks, it cannot be reconnected.

For the peridynamic fatigue parameters A and m provided in Eq. (4.1a), the parameters have different values in each phase of fatigue failure, such as crack nucleation and crack growth. The life reduction ratio of bond in the phase of crack nucleation can be described as

$$\frac{d\lambda_{(k)(j)}}{dN} = -A_1\left(\varepsilon_{(k)(j)}\right)^{m_1} \tag{4.5}$$

where A_1 and m_1 are peridynamic fatigue parameters for crack nucleation.

The parameters A_1 and m_1 can be calibrated from experimental data. For a bond with the largest cyclic bond strain ε_1 in a material undergoing repeated loadings, the bond will be broken, and the damage will initiate at this broken bond. The number of cycles to the first bond breakage N_1 can be calculated by integrating Eq. (4.5) over N as

$$\int_1^0 d\lambda_1 = \int_0^{N_1} -A_1(\varepsilon_1)^{m_1} dN \tag{4.6a}$$

and

$$0 - 1 = -A_1(\varepsilon_1)^{m_1} N_1 \tag{4.6b}$$

which results in

$$A_1 \varepsilon_1{}^{m_1} N_1 = 1 \tag{4.7}$$

where λ_1 is the remaining life of the bond which will break first and ε_1 is the cyclic bond strain of the bond which will break first. Therefore, the crack nucleation occurs at

$$N_1 = \frac{1}{A_1 \varepsilon_1{}^{m_1}} \tag{4.8}$$

Eq. (4.8) can be represented on logarithmic scale as

$$log N_1 = -log A_1 - m_1 log \varepsilon_1 \tag{4.9a}$$

and

$$log \varepsilon_1 = -\frac{1}{m_1} log N_1 - \frac{1}{m_1} log A_1 \tag{4.9b}$$

The parameters A_1 and m_1 can be determined by fitting a straight line to experimental data, which is a Strain-Life curve on logarithmic scale as shown in Fig. 4.2 [13].
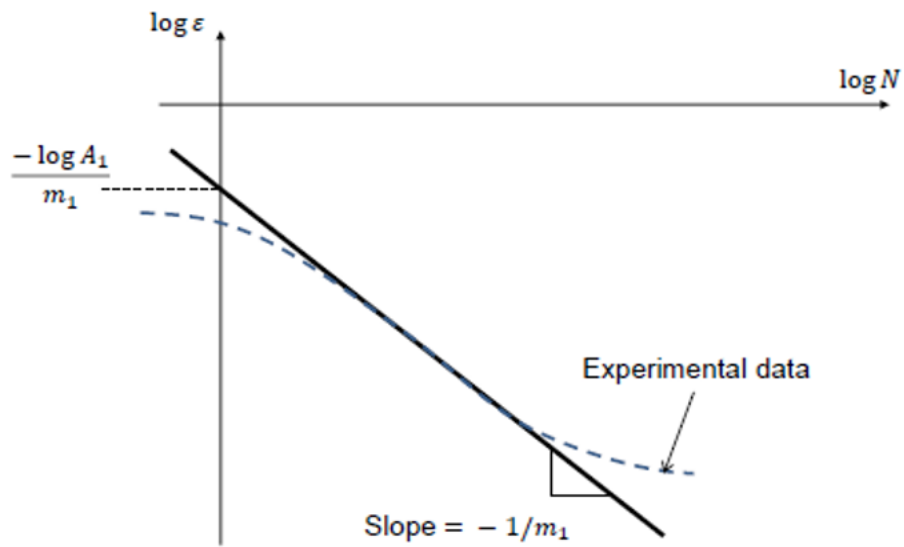
Figure 4.2. Calibration of peridynamic fatigue parameters A_1 and m_1 [34]

The expression of Eq. (2.1b) can be expressed in terms of strain rather than stress as

$$logN_f = logC_f - m_f log\Delta\varepsilon \qquad (4.10)$$

where N_f is the number of cycles to failure, $\Delta\varepsilon$ is the strain range, C_f and m_f are constants. If the fatigue constants C_f and m_f of the strain-life curve for a material are provided, the parameters A_1 and m_1 can be easily obtained by comparing Eq. (4.9a) with Eq. (4.10). the parameters A_1 and m_1 are represented as

$$m_1 = m_f \qquad (4.11a)$$

and

$$A_1 = \frac{1}{C_f} \qquad (4.11b)$$

4.3 Crack growth

For a material with a pre-existing crack undergoing repeated loadings, the remaining life of all bonds in the vicinity of a crack tip is calculated by rewriting Eq. (4.1a) as

$$\frac{d\lambda_{(k)(j)}}{dN} = -A_2 \left(\varepsilon_{(k)(j)} \right)^{m_2} \tag{4.12}$$

where A_2 and m_2 are the peridynamic fatigue parameters for the phase of crack growth. The parameters A_2 and m_2 are only valid for bonds within the horizon of the crack tip.

It is assumed that the crack propagates a constant crack growth rate in each load cycle [13]. Therefore, the bond cyclic strain and the remaining life of bonds near the crack tip are represented as a function of position relative to the crack tip as [13]

$$\varepsilon = \bar{\varepsilon}(z) \tag{4.13}$$

and

$$\lambda = \bar{\lambda}(z) \tag{4.14}$$

where z is the position coordinate based on the crack tip along the mode-1 crack axis, which is shown in Fig. 4.3, $\bar{\varepsilon}$ is the cyclic bond strain and $\bar{\lambda}$ is the remaining life functions of position relative to the crack tip.
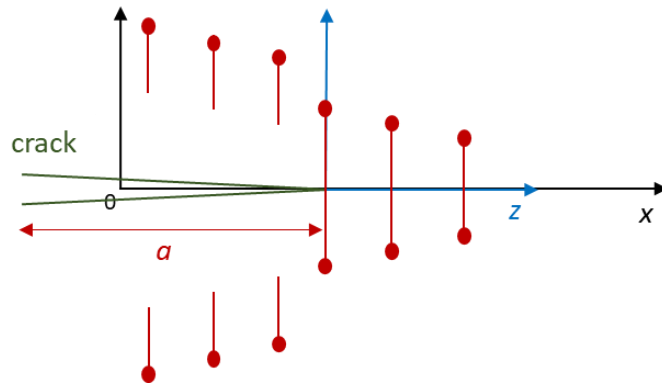
Figure 4.3 z-coordinate along the mode-1 crack axis of x-coordinate

As the crack grows, the position of crack tip can be expressed as [13]

$$z = x - \frac{da}{dN} N \tag{4.15}$$

where x is the spatial coordinate along the mode-1 crack axis, and a is the crack length.

The remaining life of bonds at the boundary $z = \delta$ (Fig. 4.1) can be calculated by integrating the derivative of Eq. (4.14) over z as

$$\int_0^\delta d\bar{\lambda} = \int_0^\delta \frac{d\bar{\lambda}}{dz} dz \tag{4.16a}$$

and

$$\bar{\lambda}(\delta) - \bar{\lambda}(0) = \int_0^\delta \frac{d\bar{\lambda}}{dz} dz \tag{4.16b}$$

which results in

$$\bar{\lambda}(\delta) = \bar{\lambda}(0) + \int_0^\delta \frac{d\bar{\lambda}}{dz} dz = \bar{\lambda}(0) + \int_0^\delta \frac{d\bar{\lambda}}{dN} \frac{dN}{dz} dz \tag{4.17}$$

Differentiating Eq. (4.15) with respect to z leads to

$$\frac{dN}{dz} = -\frac{1}{da/dN} \tag{4.18}$$

Substituting Eq. (4.12), (4.13) and (4.18) into Eq. (4.17) leads to

$$\bar{\lambda}(\delta) = \bar{\lambda}(0) + \frac{A_2}{da/dN} \int_0^\delta (\bar{\varepsilon}(z))^{m_2} dz \tag{4.19}$$

For a bond at the boundary of crack tip area, because Eq. (4.12) is only valid for bonds within a crack tip area, the remaining life of bonds at the boundary $z = \delta$ is not reduced by the phase of crack growth. Therefore, the remaining life of bonds at the boundary becomes

$$\bar{\lambda}(\delta) = 1 \tag{4.20}$$

For a bond at the crack tip, because the bond is on the verge of breakage, it is considered as the most recently broken bond. Therefore, the remaining life of the bond at the crack tip $z = 0$ becomes

$$\bar{\lambda}(0) = 0 \tag{4.21}$$

Silling and Askari [13] assumed that the cyclic bond strain can be expressed as

$$\varepsilon = \bar{\varepsilon}(z) = \bar{\varepsilon}(0)f(z) \tag{4.22}$$

where f is the function to represent the distribution around a crack tip, which, for the mode-1 crack tip, the function is independent of loading, and has a value of zero sufficiently near the origin $z = 0$ [13]. Substituting Eq. (4.20), (4.21) and (4.22) into Eq. (4.19) leads to

$$1 = 0 + \frac{A_2}{da/dN} \int_0^\delta (\bar{\varepsilon}(0)f(z))^{m_2} \, dz \tag{4.23}$$

From Eq. (4.23), the crack growth rate can be represented as below

$$\frac{da}{dN} = \beta A_2 (\bar{\varepsilon}(0))^{m_2} \tag{4.24a}$$

and

$$\beta = \int_0^\tau (f(z))^{m_2} dz \tag{4.24b}$$

The parameter m_2 can be determined by comparing Eq. (4.24a) with Eq. (2.4). Because, $\bar{\varepsilon}(0)$ is proportional to the cyclic stress intensity factor ΔK in Eq. (2.4), and C and M are constants in Eq. (2.4), the exponents of Eq. (4.24a) and (2.4) are same in both expressions as [13]

$$m_2 = M \tag{4.25}$$

the parameter m_2 is easily calibrated from experimental data of Paris curve, which the fatigue constants C and M are values calibrated by experimental tests. However, it is difficult to calibrate directly the parameter A_2 from the Paris curve because of unknown parameters β and $\bar{\varepsilon}(0)$. To calibrate the parameter A_2, it is necessary to perform a peridynamic simulation with an arbitrary parameter A_2'. A numerical result of fatigue crack growth rate $\left(\frac{da}{dN}\right)'$ can be obtained from the peridynamic simulation with an arbitrary parameter A_2'.

The relation between the authentic parameter A_2 and the arbitrary parameter A_2' can be derived from Eq. (4.24a) as

$$\frac{da/dN}{A_2} = \beta(\bar{\varepsilon}(0))^{m_2} \tag{4.26a}$$

and

$$\frac{(da/dN)'}{A_2'} = \beta(\bar{\varepsilon}(0))^{m_2} \tag{4.26b}$$

which results in

$$A_2 = A_2' \frac{da/dN}{(da/dN)'} \qquad (4.27)$$

From Eq. (2.4) and (4.27), the parameter A_2 is expressed as below [13]

$$A_2 = A_2' \frac{da/dN}{(da/dN)'} = A_2' \frac{C\Delta K^M}{(da/dN)'} \qquad (4.28)$$

A process of peridynamic simulation to calibrate the parameter A_2 is described in Chapter 5.3.3.1.

5. FATIGUE DAMAGE SIMULATION

This chapter presents peridynamic computational approaches to simulate two phases of fatigue failure: crack nucleation and crack growth by using peridynamic fatigue model proposed by Silling and Askari [13]. All simulations are treated as quasi-static bond-based peridynamic theory. Also, it is assumed that all material behaviour in peridynamic calculations are linear elastic material behaviour.

Typically, the peridynamic motion equation takes dynamic forms and can be solved by using explicit time integration as described in Chapter 3. However, for a stable calculation, a small time step is generally required. Since the fatigue processes generally take place for a long period, it is too heavy to simulate fatigue failures with an extremely small time step. Therefore, to avoid computational costs, all simulations are treated as quasi-static.

5.1 Peridynamic static solution

There are some techniques to obtain static or quasi-static solutions. One of the most common methods is the adaptive dynamic relaxation (ADR) technique. Kilic and Madenci [35] proposed this method by introducing an artificial damping to the peridynamic equation to obtain static or quasi-static solutions, which a static solution can be considered as a part of steady-state in dynamic solution. The other technique is solving directly a peridynamic static equation, which is available only in solving a linear system equation as a matrix form [36]. In this study, all peridynamic quasi-static solutions are obtained by using a direct static solution method.

The static equation of peridynamic theory can be obtained by setting the acceleration term to 0 in Equation (3.1) as

$$\int_{H_{\mathbf{x}}} \mathbf{f}(\mathbf{u}(\mathbf{x}', t) - \mathbf{u}(\mathbf{x}, t), \mathbf{x}' - \mathbf{x})dV_{\mathbf{x}'} + \mathbf{b}(\mathbf{x}, t) = 0 \qquad (5.1)$$

where $H_{\mathbf{x}}$ is the horizon of the material point $\mathbf{x}$, $\mathbf{u}$ is the displacement vector field, $\mathbf{f}$ is the pairwise force function which represents the force per unit volume, which the material point k exerts on the material point j, and $\mathbf{b}$ is a exerted body force density.

For a linear elastic material, the peridynamic force can be expressed in a linearized function as [32]

$$\mathbf{f}(\mathbf{u}(\mathbf{x}', t) - \mathbf{u}(\mathbf{x}, t), \mathbf{x}' - \mathbf{x}) = \mathbf{C}(\boldsymbol{\xi})\boldsymbol{\eta} \tag{5.2a}$$

$$\boldsymbol{\xi} = \mathbf{x}' - \mathbf{x} \tag{5.2b}$$

$$\boldsymbol{\eta} = \mathbf{u}(\mathbf{x}', t) - \mathbf{u}(\mathbf{x}, t) \tag{5.2c}$$

where $\boldsymbol{\xi}$ is relative position between material points $\mathbf{x}$ and $\mathbf{x}'$, $\boldsymbol{\eta}$ is relative displacement between material points $\mathbf{x}$ and $\mathbf{x}'$ and $\mathbf{C}$ is a second-order material's micromodulus tensor given by [32]

$$\mathbf{C}(\boldsymbol{\xi}) = \frac{\partial \mathbf{f}}{\partial \boldsymbol{\eta}}(0, \boldsymbol{\xi}) \tag{5.3}$$

The micromodulus tensor can be expressed as [37]

$$\mathbf{C}(\boldsymbol{\xi}) = \frac{c}{|\boldsymbol{\xi}|} \mathbf{M} \otimes \mathbf{M} \tag{5.4}$$

where c is the bond constant, $\otimes$ is the operator of dyadic product, and $\mathbf{M}$ is the unit vector of bond direction in the reference configuration, which is given as [36]

$$\mathbf{M} = \frac{\boldsymbol{\xi}}{|\boldsymbol{\xi}|} \tag{5.5}$$

Substituting Eq. (5.4) and (5.5) into Eq. (5.2a) leads to [36]

$$\mathbf{f} = c \frac{\boldsymbol{\xi} \otimes \boldsymbol{\xi}}{|\boldsymbol{\xi}|^3} \boldsymbol{\eta} \qquad (5.6)$$

which $\mathbf{f}$ is the peridynamic force in the microelastic material. It can be expressed in a matrix form as [36]

$$\begin{Bmatrix} f_x \\ f_y \\ f_z \end{Bmatrix} = \frac{c}{|\boldsymbol{\xi}|^3} \begin{bmatrix} \xi_x \xi_x & \xi_x \xi_y & \xi_x \xi_z \\ \xi_y \xi_x & \xi_y \xi_y & \xi_y \xi_z \\ \xi_z \xi_x & \xi_z \xi_y & \xi_z \xi_z \end{bmatrix} \begin{Bmatrix} \eta_x \\ \eta_y \\ \eta_z \end{Bmatrix} \qquad (5.7)$$

Where c is the bond constant and subscripts of $\mathbf{f}$, ξ, and η indicate components of x, y and z axis. Eq. (5.7) can be expressed in two dimensional as [36]

$$\begin{Bmatrix} f_x \\ f_y \end{Bmatrix} = \frac{c}{|\boldsymbol{\xi}|^3} \begin{bmatrix} \xi_x \xi_x & \xi_x \xi_y \\ \xi_y \xi_x & \xi_y \xi_y \end{bmatrix} \begin{Bmatrix} \eta_x \\ \eta_y \end{Bmatrix} \qquad (5.8)$$

where ξ_x and ξ_y can be represented as below

$$\xi_x = |\boldsymbol{\xi}| cos\theta \qquad (5.9a)$$

and

$$\xi_x = |\boldsymbol{\xi}| sin\theta \qquad (5.9b)$$

where θ is the angle of bond from the x-axis in the reference configuration.

Substituting Eq. (5.9a) and (5.9b) into Eq. (5.8) leads to

$$\begin{Bmatrix} f_x \\ f_y \end{Bmatrix} = \frac{c}{|\xi|} \begin{bmatrix} \cos^2\theta & \cos\theta\sin\theta \\ \sin\theta\cos\theta & \sin^2\theta \end{bmatrix} \begin{Bmatrix} \eta_x \\ \eta_y \end{Bmatrix} \tag{5.10}$$

To solve the peridynamic static equation, it is necessary to be represented in discretized form for numerical calculation as

$$\sum_{j=1}^{Q} \mathbf{f}\left(\mathbf{u}_{(j)} - \mathbf{u}_{(k)}, \mathbf{x}_{(j)} - \mathbf{x}_{(k)}\right) V_{(j)} + \mathbf{b}_{(k)} = 0 \tag{5.11}$$

where Q is the number of material points within the horizon of the material point k. Substituting Eq. (5.10) into Eq. (5.11) leads to

$$\sum_{j=1}^{Q} \frac{c}{|\xi_{(k)(j)}|} \begin{bmatrix} \cos^2\theta_{(k)(j)} & \cos\theta_{(k)(j)}\sin\theta_{(k)(j)} \\ \sin\theta_{(k)(j)}\cos\theta_{(k)(j)} & \sin^2\theta_{(k)(j)} \end{bmatrix} \begin{Bmatrix} \eta_{(k)(j)_x} \\ \eta_{(k)(j)_y} \end{Bmatrix} V_j + \begin{Bmatrix} b_{(k)_x} \\ b_{(k)_y} \end{Bmatrix}$$
$$= 0 \tag{5.12}$$

where $\theta_{(k)(j)}$ is the angle of bond between two material points k and j from the x-axis in the reference configuration, $b_{(k)_x}$ and $b_{(k)_y}$ are the x-component and y-component of $\mathbf{b}_{(k)}$, respectively. $\eta_{(k)(j)_x}$ and $\eta_{(k)(j)_y}$ can be represented as

$$\eta_{(k)(j)_x} = u_{(j)_x} - u_{(k)_x} \tag{5.13a}$$

and

$$\eta_{(k)(j)_y} = u_{(j)_y} - u_{(k)_y} \tag{5.13b}$$

where $u_{(k)_x}$ and $u_{(k)_y}$ are the x-component and y-component of $\mathbf{u}_{(k)}$, respectively. By using Eq. (5.13a) and (5.13b), Eq. (5.12) can be expressed in a matrix form consisting of each component displacement of material points k and j as [36]

$$\sum_{j=1}^{Q} \frac{c}{|\xi_{(k)(j)}|} \begin{bmatrix} cos^2\theta & cos\theta sin\theta & -cos^2\theta & -cos\theta sin\theta \\ sin\theta cos\theta & sin^2\theta & -sin\theta cos\theta & -sin^2\theta \end{bmatrix} \begin{Bmatrix} u_{(k)_x} \\ u_{(k)_y} \\ u_{(j)_x} \\ u_{(j)_y} \end{Bmatrix} V_j$$

$$= \begin{Bmatrix} b_{(k)_x} \\ b_{(k)_y} \end{Bmatrix} \quad (5.14a)$$

and

$$\begin{bmatrix} \mathbf{K}_{(2k-1)(2k-1)} & \mathbf{K}_{(2k)(2k-1)} & \mathbf{K}_{(2k-1)(2j-1)} & \mathbf{K}_{(2k-1)(2j)} \\ \mathbf{K}_{(2k)(2k-1)} & \mathbf{K}_{(2k)(2k-1)} & \mathbf{K}_{(2k)(2j-1)} & \mathbf{K}_{(2k)(2j)} \end{bmatrix} \begin{Bmatrix} u_{(k)_x} \\ u_{(k)_y} \\ u_{(j)_x} \\ u_{(j)_y} \end{Bmatrix}$$

$$= \begin{Bmatrix} b_{(k)_x} \\ b_{(k)_y} \end{Bmatrix} \quad (5.14b)$$

where $\theta = \theta_{(k)(j)}$. Considering all material points with Eq. (5.14b) leads to a global matrix form as

$$\begin{bmatrix} \mathbf{K}_{(1)(1)} & \mathbf{K}_{(1)(2)} & \mathbf{K}_{(1)(3)} & \mathbf{K}_{(1)(4)} & \cdots & \mathbf{K}_{(1)(2N_t)} \\ \mathbf{K}_{(2)(1)} & \mathbf{K}_{(2)(2)} & \mathbf{K}_{(2)(3)} & \mathbf{K}_{(2)(4)} & \cdots & \mathbf{K}_{(2)(2N_t)} \\ \mathbf{K}_{(3)(1)} & \mathbf{K}_{(3)(2)} & \mathbf{K}_{(1)(3)} & \mathbf{K}_{(1)(4)} & \cdots & \mathbf{K}_{(3)(2N_t)} \\ \mathbf{K}_{(4)(1)} & \mathbf{K}_{(4)(2)} & \mathbf{K}_{(2)(3)} & \mathbf{K}_{(2)(4)} & \cdots & \mathbf{K}_{(4)(2N_t)} \\ \vdots & \vdots & & \vdots & \vdots & \ddots & \vdots \\ \mathbf{K}_{(2N_t)(1)} & \mathbf{K}_{(2N_t)(2)} & \mathbf{K}_{(2N_t)(3)} & \mathbf{K}_{(2N_t)(4)} & \cdots & \mathbf{K}_{(2N_t)(2N_t)} \end{bmatrix} \begin{Bmatrix} u_{(1)_x} \\ u_{(1)_y} \\ u_{(2)_x} \\ u_{(2)_y} \\ \vdots \\ u_{(N_t)_x} \\ u_{(N_t)_y} \end{Bmatrix} = \begin{Bmatrix} b_{(1)_x} \\ b_{(1)_y} \\ b_{(2)_x} \\ b_{(2)_y} \\ \vdots \\ b_{(N_t)_x} \\ b_{(N_t)_y} \end{Bmatrix} \quad (5.15)$$

where N_t is the total number of material points in the material, and $\mathbf{K}_{ij}$ is the component of global stiffness matrix.

The global matrix equation of Eq. (5.15) can be expressed as

$$\mathbf{K_G U_G = F_G} \tag{5.16}$$

where $\mathbf{K_G}$ is the global stiffness matrix, $\mathbf{U_G}$ is the global displacement matrix, and $\mathbf{F_G}$ is the global body force vector. The global displacement matrix $\mathbf{U_G}$ can be directly obtained by taking the inverse of global stiffness matrix as

$$\mathbf{U_G = {K_G}^{-1} F_G} \tag{5.17}$$

5.2 Fatigue crack nucleation

To validate the peridynamic fatigue model in crack nucleation phase, the fatigue crack nucleation is simulated. Fatigue tensile tests are simulated with a two-dimensional numerical model under uniaxial tension-compression loadings for 7075-T651 aluminium alloy.

5.2.1 Numerical model for crack nucleation

A two-dimensional plate model which is made of 7075-T651 aluminium alloy is used to represent crack nucleation. Mechanical material properties of 7075-T651 aluminium alloy are given in Table.5.1. A geometry of the numerical model is represented in Fig. 5.1. The numerical model is subjected to uniaxial tension-compression cyclic loadings at the top and bottom. Loading conditions are described in Table 5.2 and Fig. 5.2.

Boundary conditions:

- $u_y = 0$ at $y = 0$
- $u_x = 0$ at $y = 0$ and $x = 0$

Loading conditions:

- Uniaxial cyclic loading σ (MPa) at $y = \pm 54.75\ mm$

Thickness of the plate:

- $3.6\ mm$

Table 5.1. Mechanical properties of 7075-T651 aluminium alloy [38]

Elasticity modulus, E	71.7 GPa
Poisson's ratio, v	0.33
Yield stress, σ_Y	501 MPa
Ultimate strength, σ_u	561 MPa
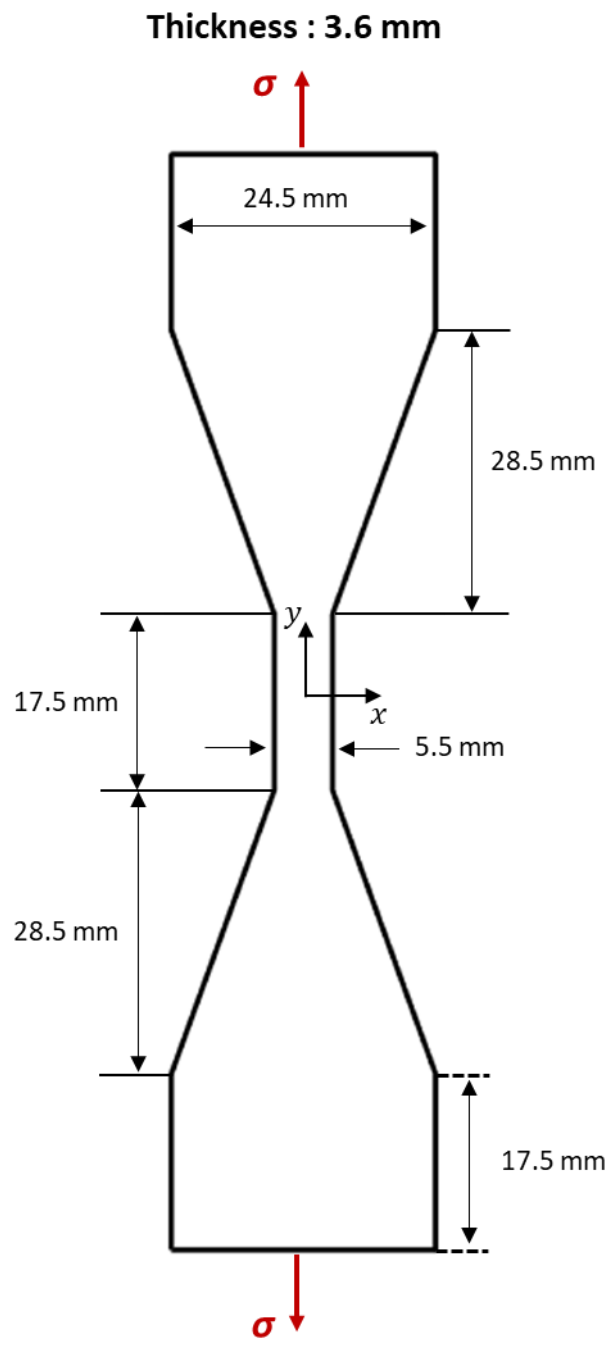
Figure 5.1. Geometry of numerical model for fatigue crack nucleation under uniaxial tension-compression cyclic loading

Table 5.2. Loading conditions for numerical fatigue tensile tests [38]

Case	Stress amplitude (MPa)	Mean stress (MPa)	Frequency (Hz)	Load ratio
1	368.8	-54.4	1	-1
2	333.2	-22.2	2	-1
3	299.3	1.3	4	-1
4	262.4	1.2	5	-1
5	222.1	1.0	10	-1
6	210.2	15.5	10	-1
7	191.4	0.7	10	-1
8	157.0	0.7	5	-1
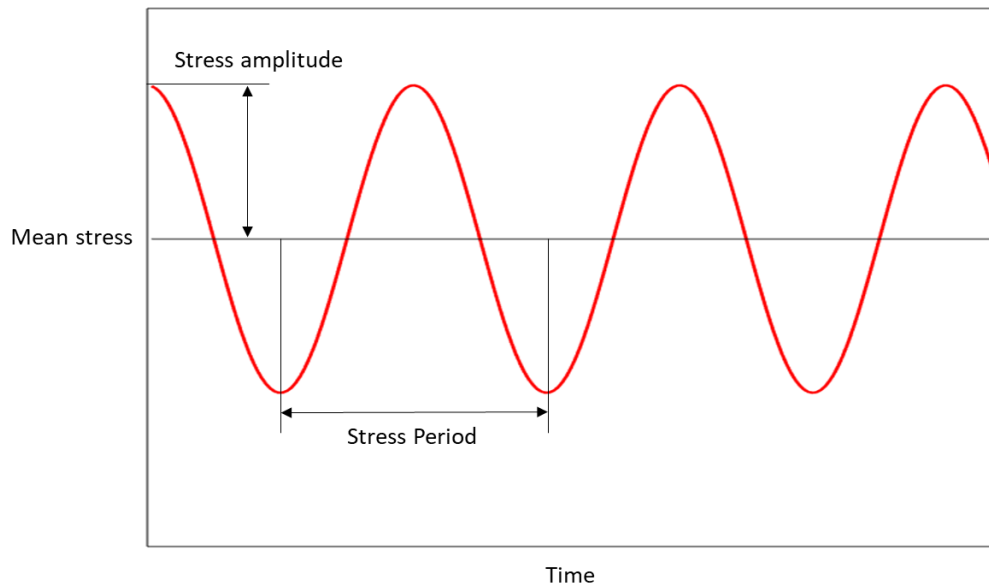
Figure 5.2 Fully reversed uniaxial loadings ($R = -1$) as a function of time for crack nucleation

5.2.2 Numerical procedure for crack nucleation simulation

A numerical procedure for simulating crack nucleation is described in Fig. 5.3.
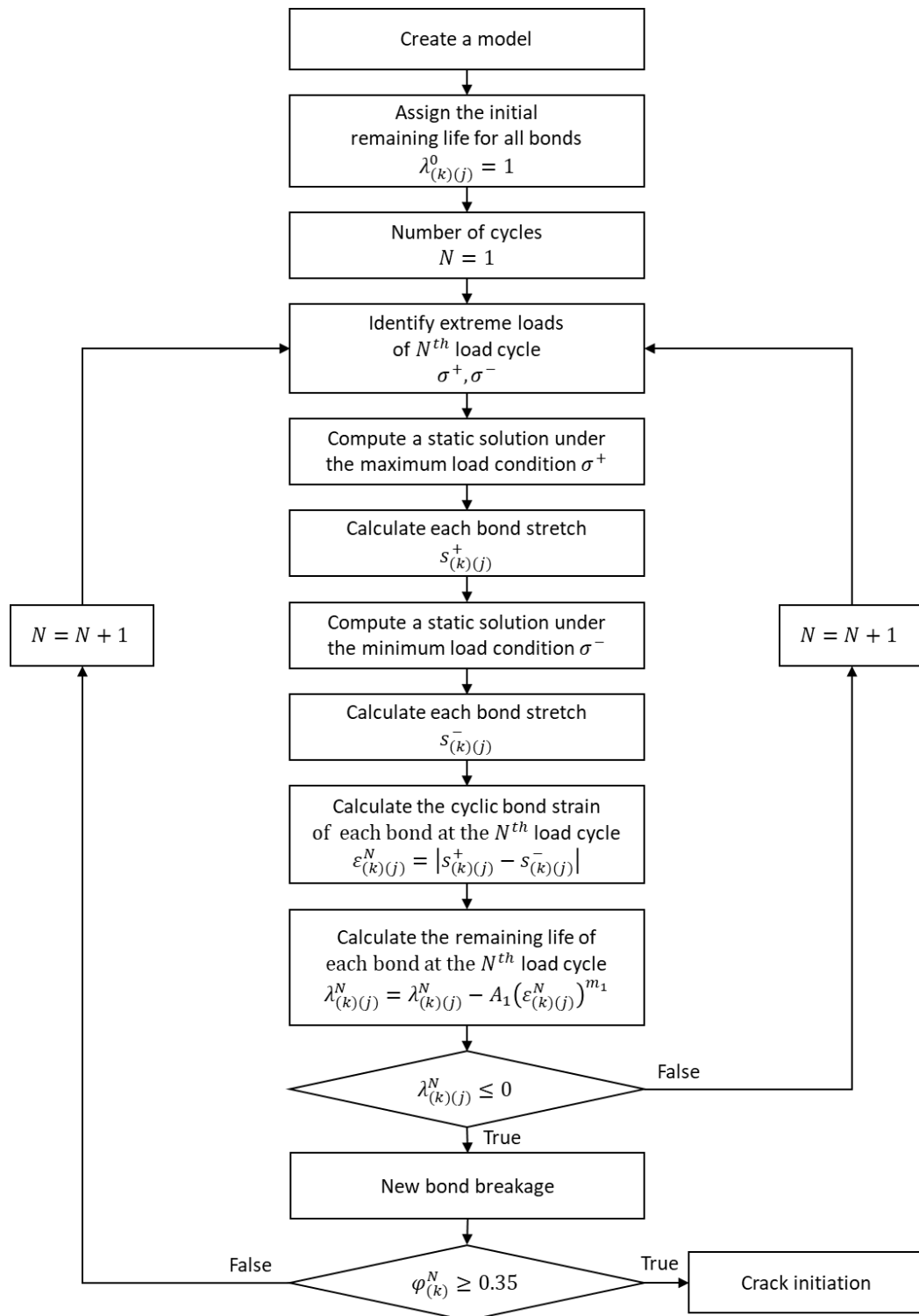
Figure 5.3. Flowchart for simulation of fatigue crack nucleation

The numerical procedure for simulating crack nucleation is described as

1) Create a model

   Firstly, it is necessary to discretize a geometry of model into material points for the peridynamic calculation. Also, peridynamic parameters for the peridynamic calculation should be identified based on material properties, such as bond constant, critical bond stretch and peridynamic fatigue parameters.

2) Assign the initial remaining life

   All bonds in a material have an initial value of remaining life at the initial state before applying cycle loads (Eq. (4.1b)).

3) Identify extreme loads of the Nth load cycle

   In order to calculate the fatigue damage during the Nth load cycle, it is necessary to identify two extremes in the Nth load cycle. Fig. 5.4 shows the maximum and minimum points in each load cycle, which the only two extremes are required to calculate the Nth cyclic bond strain in the Nth load cycle.

4) Compute two static solutions under each extreme load condition

   Peridynamic static solutions under each extreme load condition can be calculated by direct solution as described in Chapter 5.1.
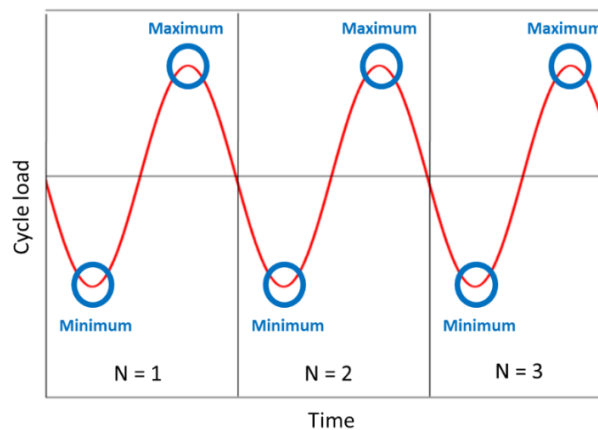
Figure 5.4 Maximum and minimum loads in each load cycle

5) Calculate the cyclic bond strain of each bond at the Nth load cycle

The maximum and minimum bond stretches $s^{+}_{(k)(j)}$ and $s^{-}_{(k)(j)}$ between material points k and j at the Nth load cycle can be calculated respectively based on the peridynamic static solutions. With the maximum and minimum bond stretches, the cyclic bond strain of each bond at the Nth load cycle can be calculated from Eq. (4.2).

6) Calculate the remaining life of each bond at the Nth load cycle

The remaining life of each bond at the Nth load cycle can be calculated by integrating Eq. (4.5) as

$$\int_{\lambda^{N-1}_{(k)(j)}}^{\lambda^{N}_{(k)(j)}} d\lambda_{(k)(j)} = \int_{N-1}^{N} -A_1\left(\varepsilon^{N}_{(k)(j)}\right)^{m_1} dN \qquad (5.18a)$$

and

$$\lambda^{N}_{(k)(j)} = \lambda^{N-1}_{(k)(j)} - A_1\left(\varepsilon^{N}_{(k)(j)}\right)^{m_1} \qquad (5.18b)$$

where N is the number of cycles, $\lambda^{N}_{(k)(j)}$ and $\varepsilon^{N}_{(k)(j)}$ are remaining life and cyclic bond strain of bond between material points k and j at the Nth load cycle, respectively. A_1 and m_1 are the peridynamic fatigue parameters. When the remaining life of bond is 0 or less than 0, $(\lambda^{N}_{(k)(j)} \leq 0)$, a new bond breakage occurs.

7) Crack initiation

When the local damage of any material points $\varphi^{N}_{(k)}$ is 0.35 or greater than 0.35, it is assumed that the crack has occurred at that material point [39]. Once the crack occurs in the material, it is required to be treated as the pre-existing crack problem. Therefore, it is necessary for bonds near crack tips to be shifted to the crack growth phase for the proper simulation.

5.2.3 Peridynamic simulation for crack nucleation

A discretization of two-dimensional model is represented in Fig. 5.5, which the R_b indicates the material points where body forces are applied. Peridynamic parameters are represented as

- Total number of material points: 7385
- Spacing between material points: Δ= 0.5 mm
- Thickness: $t = 3.6$ mm
- Incremental volume of material points: $\Delta V = t \times \Delta \times \Delta$= 0.9 mm^3
- Horizon: $3.015 \times \Delta$= 1.5075 mm
- Critical bond stretch: $s_0 = 0.01$
- Static solution: Direct solution
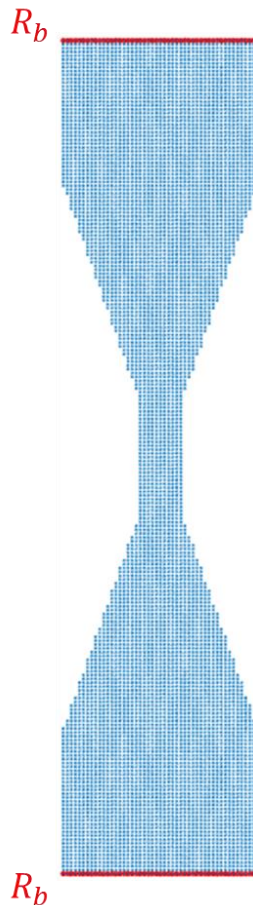
Figure 5.5. Geometry of numerical model for fatigue crack nucleation and its discretization

5.2.3.1 Calibration of peridynamic fatigue parameters for crack nucleation

The 7075-T651 aluminium alloy has a special material property called as fatigue limit, which is the minimum threshold causing the fatigue damage [38]. If the loading is less than the fatigue limit, regardless of how many loadings are applied, there is no fatigue damage. Incorporating the fatigue limit into the peridynamic fatigue model, Silling and Askari [13] modified Eq. (4.5) as below

$$\frac{d\lambda_{(k)(j)}}{dN} = \begin{cases} -A_1\big(\varepsilon_{(k)(j)} - \varepsilon_0\big)^{m_1}, & \text{if } \varepsilon_{(k)(j)} > \varepsilon_0 \\ 0, & \text{otherwise} \end{cases} \qquad (5.19)$$

where $\lambda_{(k)(j)}$ is the remaining life of bond between material points k and j, N is the number of cycles, A_1 and m_1 are the peridynamic fatigue parameters, $\varepsilon_{(k)(j)}$ is the cyclic bond strain between material points k and j, ε_0 is the fatigue limit.

To calibrate the parameters A_1 and m_1, fatigue results of Zhao and Jiang [38] are used to create a Strain-Life curve of 7075-T651 aluminium alloy. The fatigue results of Zhao and Jiang [38] and the resulting best fitting curve for the Strain-Life curve of 7075-T651 aluminium alloy are represented in Fig. 5.6. The peridynamic fatigue parameters A_1 and m_1 are calibrated by plotting the fatigue results of Zhao and Jiang [38] on logarithmic scales as shown in Fig. 5.7. The value of fatigue limit of 7075-T651 aluminium alloy is obtained from fatigue test results of Zhao and Jiang [38]. The resulting peridynamic fatigue parameters A_1 and m_1, and the fatigue limit of 7075-T651 aluminium alloy ε_0 are listed in Table 5.3.

Table 5.3. Peridynamic fatigue parameters for crack nucleation of 7075-T651

A_1	4824.11
m_1	2.8901
ε_0 [38]	0.0015
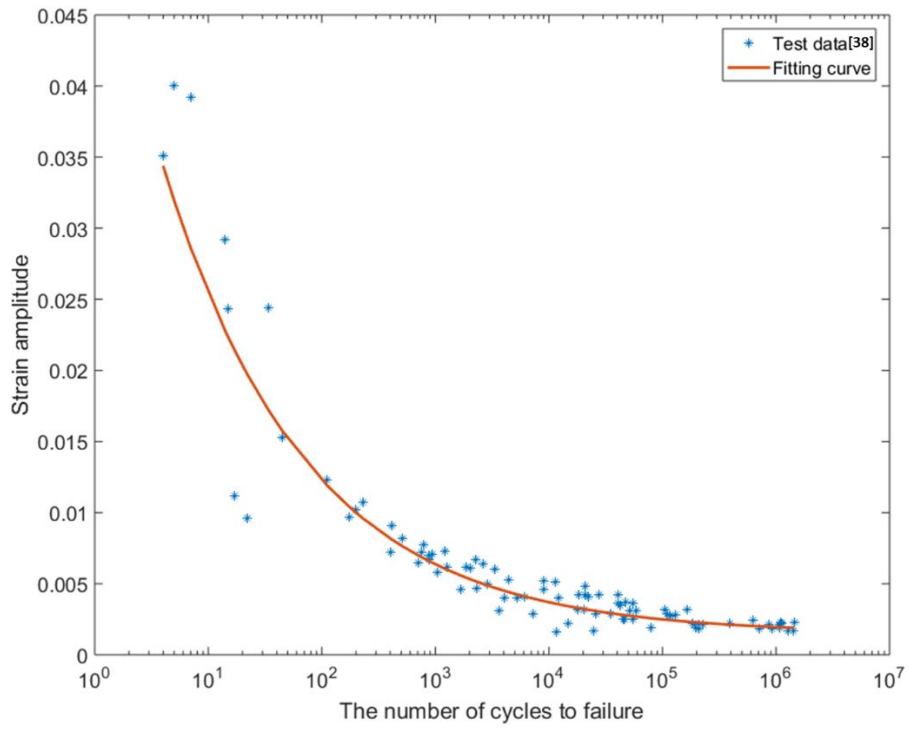
Figure 5.6. Fatigue results by Zhao and Jiang [38] and a fitting curve for Strain-Life curve
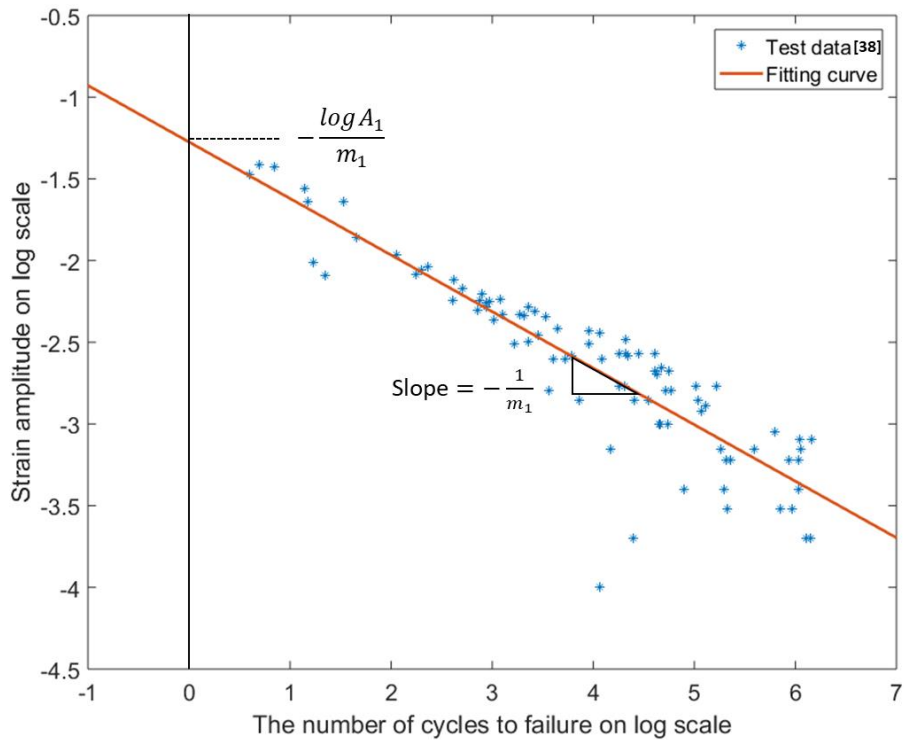
Figure 5.7. Calibration of peridynamic fatigue parameter A_1 and m_1 in logarithmic scales

5.2.4 Numerical results and validation

To validate peridynamic static solutions, first a peridynamic static solution is compared with FEM by using ANSYS software. In FEM, a plane stress element with thickness is used.

Fig. 5.8 and 5.9 show comparison between the peridynamic and the FEM static solutions under a uniaxial tension in opposite directions with forces $\sigma = 157.7$ MPa. These results show that the peridynamic results have similar displacement distributions with FEM solutions.
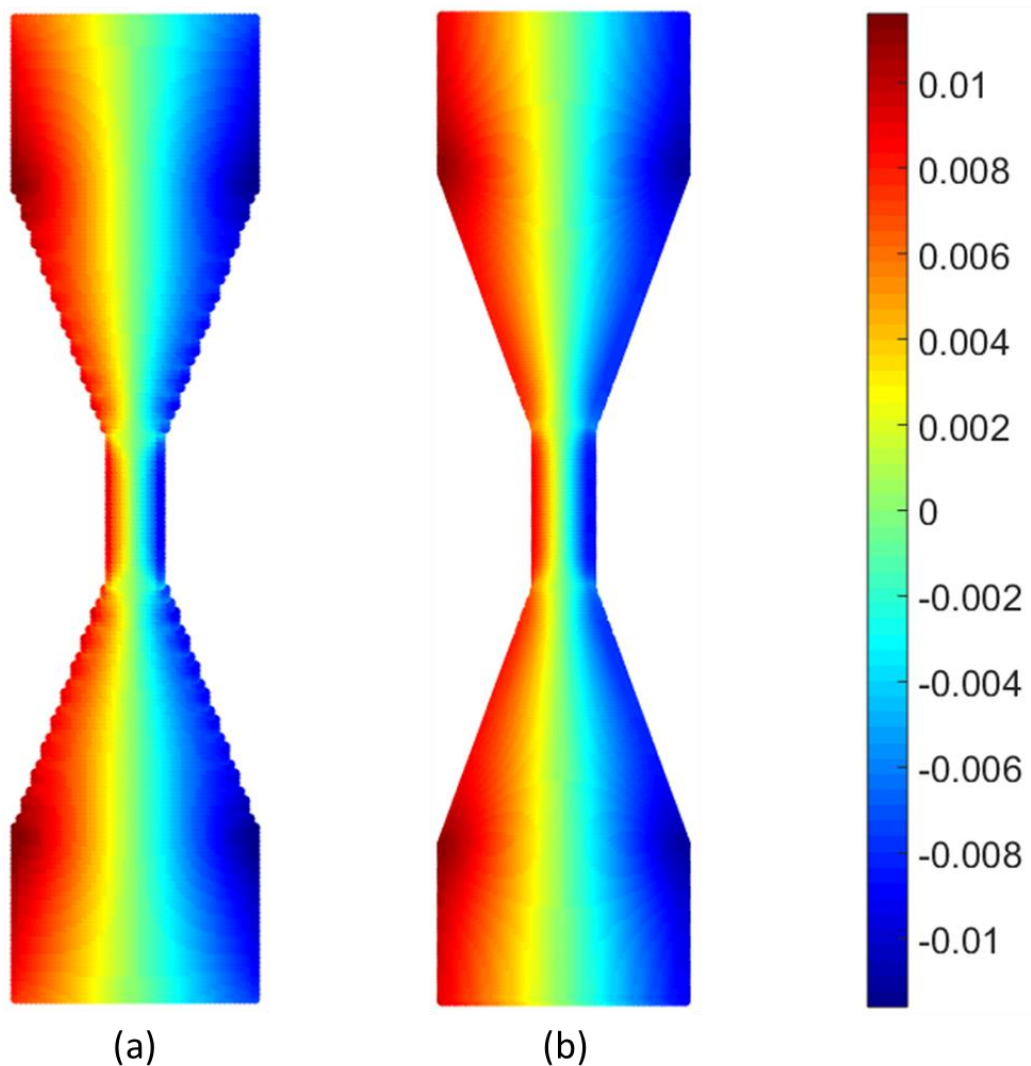
Figure 5.8. Displacement distribution in x-direction under a uniaxial tension in opposite directions with forces $\sigma = 157.7$ MPa, (a) peridynamic static solution (b) FEM static solution
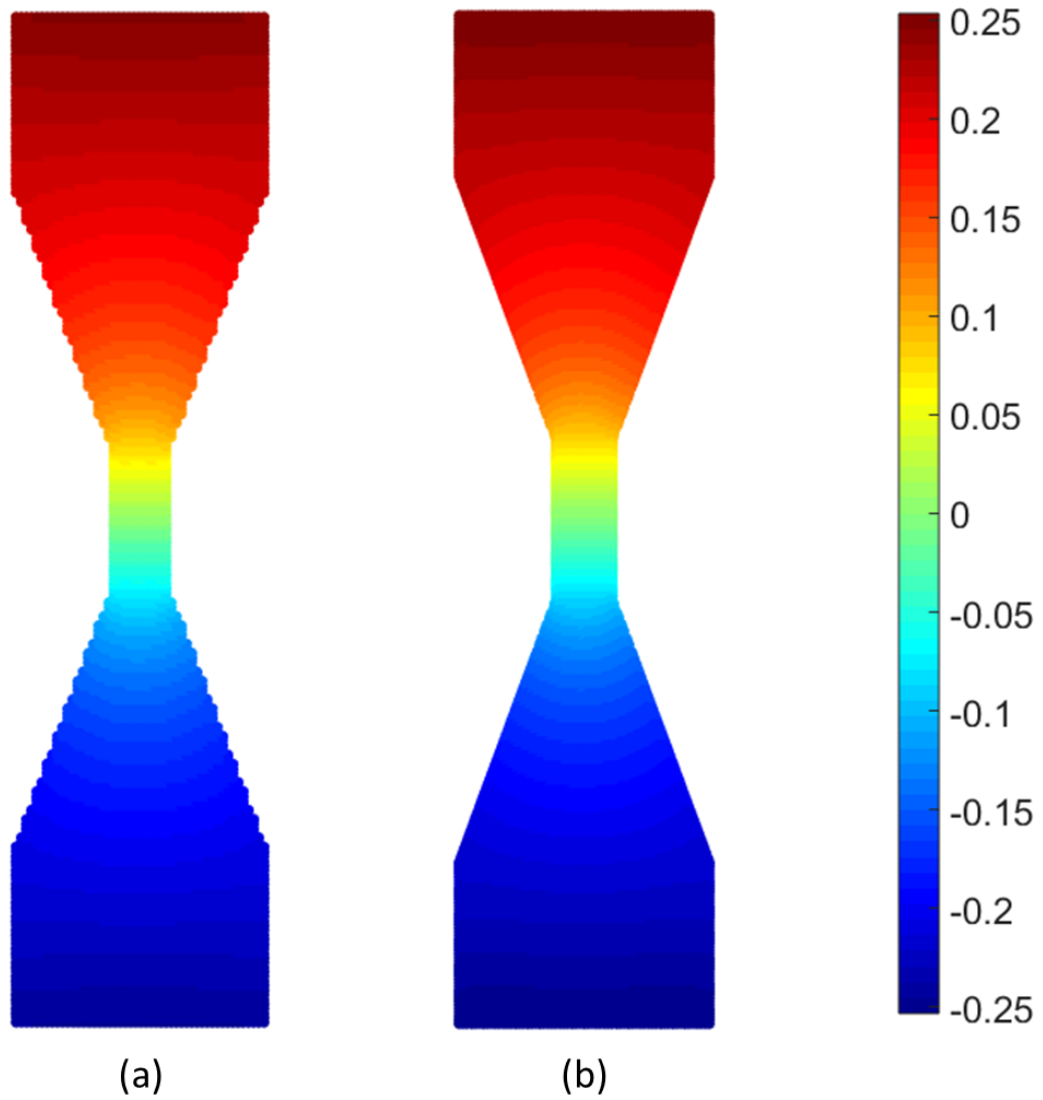
Figure 5.9. Displacement distribution in y-direction under a uniaxial tension in opposite directions with forces $\sigma = 157.7$ MPa, (a) peridynamic static solution (b) FEM static solution

After verifying the peridynamic results, simulations of fatigue crack nucleation are performed with the simulation procedure described in Chapter 5.2.2. Numerical results show that the crack nucleation occurs where there are high stress concentrations, and the fatigue damage is developed from where the crack nucleation occurs. The development of the fatigue damage is represented in Fig. 5.10. All numerical results are represented and compared with the fatigue test results by Zhao and Jiang [38] as shown in Fig. 5.11. The peridynamic fatigue model damage is calculated based on the breakage of first peridynamic bond.
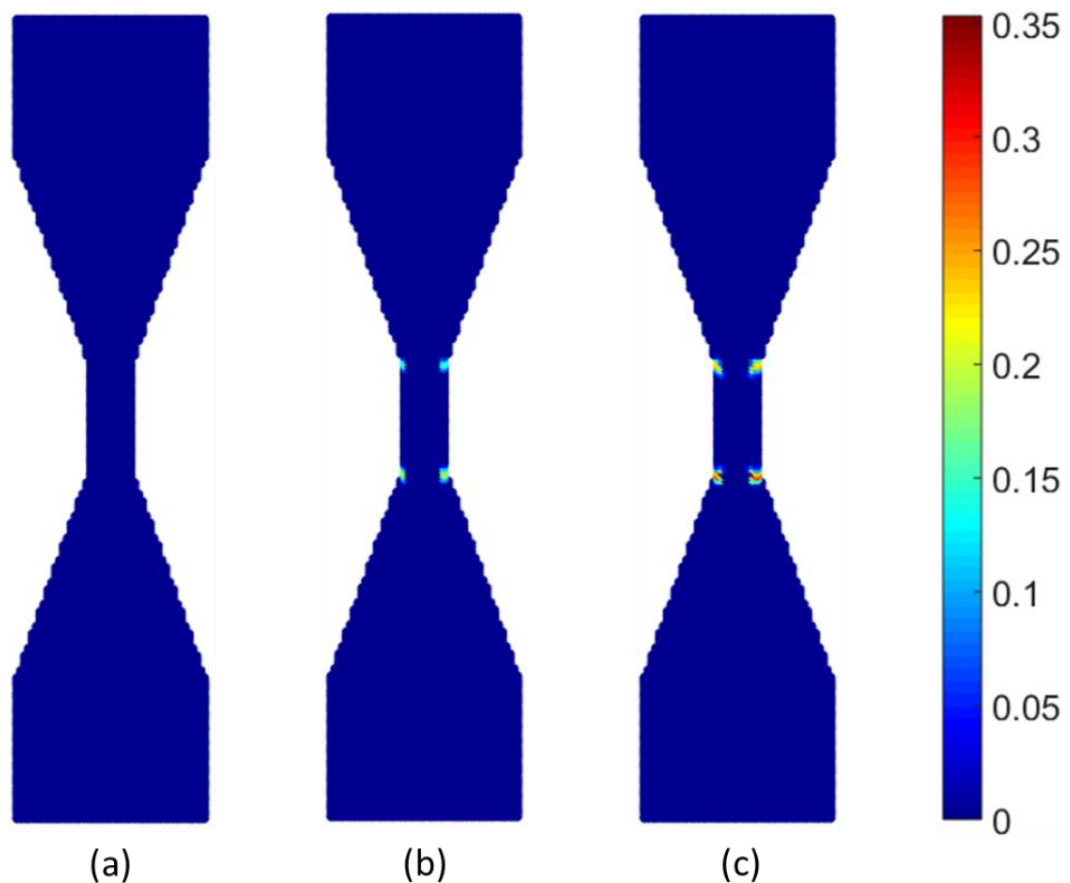
Figure 5.10. Development of fatigue damage under case 3 loading condition (Table 5.2), (a) $N = 0$, (b) $N = 2473$, (c) $N = 3863$
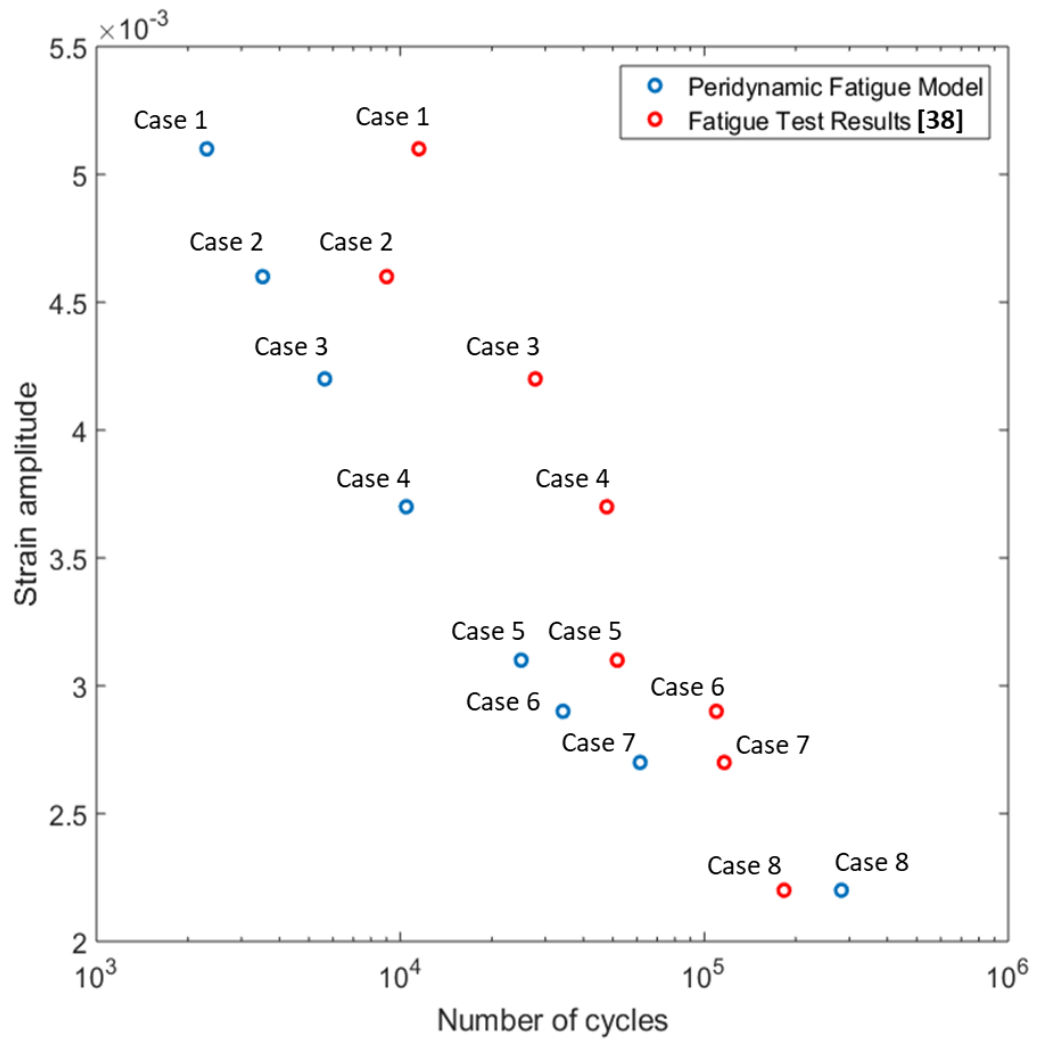
Figure 5.11. Peridynamic numerical results and comparison with fatigue test results of Zhao and Jiang [38]

5.3 Fatigue crack growth

To validate the peridynamic fatigue model in crack growth phase, the fatigue crack growth is simulated. ASTM E647 standard compact tests are simulated with a two-dimensional numerical model for 7075-T651 aluminium alloy.

5.3.1 Numerical model for crack growth

A two-dimensional plate model which is made of 7075-T651 aluminium alloy is used to represent crack growth. Mechanical material properties of 7075-T651 aluminium alloy are given in Table.5.1. A geometry of the numerical model is represented in Fig. 5.12. The numerical model is subjected to a uniaxial tension cyclic load in opposite directions at two pins of top and bottom with extreme forces $P^+ = 1500$ N and $P^- = 150$ N resulting in a load ratio of $R = 0.1$.

Boundary conditions:
- $u_x = u_y = 0$ at $y = 0$ and $x = 0$

Loading conditions:
- Uniaxial cyclic loading P (MPa) at $x = 50\ mm$ and $y = \pm 14\ mm$

Thickness of the plate:
- $6.11\ mm$
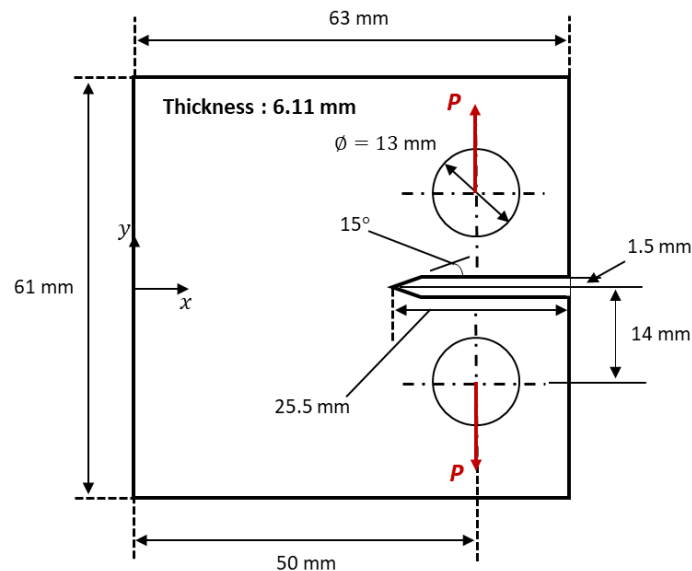
Figure 5.12. Geometry of numerical model for fatigue crack growth under uniaxial tension cyclic load

5.3.2 Numerical procedure for crack growth simulation

For a structure having a pre-existing crack, it is not suitable to simulate with the numerical procedure for crack nucleation as described in Chapter 5.2.2. Materials near a crack tip has a different mechanism from the crack nucleation phase. Crack nucleation and crack propagation are two different mechanisms. Crack propagation occurs when there is crack in the structure, and high stress concentration occurs near the crack tip which drives the crack growth. However, the crack nucleation occurs when there is no initial crack in the structure. Therefore, two different procedures are used to simulate crack initiation and propagation. The procedure for crack growth simulation is represented in Fig. 5.13.

```
┌─────────────────────────┐
│      Create a model     │
└─────────────────────────┘
            │
┌─────────────────────────┐
│  Assign the initial     │
│ remaining life for all  │
│ bonds                   │
│   λ⁰₍ₖ₎₍ⱼ₎ = 1          │
└─────────────────────────┘
            │
┌─────────────────────────┐
│   Number of cycles      │
│        N = 1            │
└─────────────────────────┘
            │
┌─────────────────────────┐
│   Define crack tip areas│
└─────────────────────────┘
            │
┌─────────────────────────┐
│  Identify extreme loads │
│   of Nᵗʰ load cycle     │
│        σ⁺, σ⁻           │
└─────────────────────────┘
            │
┌─────────────────────────┐
│ Compute a static        │
│ solution under the      │
│ maximum load condition σ⁺│
└─────────────────────────┘
            │
┌─────────────────────────┐
│ Calculate each bond     │
│ stretch                 │
│      s⁺₍ₖ₎₍ⱼ₎           │
└─────────────────────────┘
            │
┌─────────────────────────┐
│ Compute a static        │
│ solution under the      │
│ minimum load condition σ⁻│
└─────────────────────────┘
            │
┌─────────────────────────┐
│ Calculate each bond     │
│ stretch                 │
│      s⁻₍ₖ₎₍ⱼ₎           │
└─────────────────────────┘
```

Assign the initial remaining life for all bonds
$$\lambda^0_{(k)(j)} = 1$$

Number of cycles
$$N = 1$$

Define crack tip areas

Identify extreme loads of Nth load cycle
$$\sigma^+, \sigma^-$$

Compute a static solution under the maximum load condition σ^+

Calculate each bond stretch
$$s^+_{(k)(j)}$$

Compute a static solution under the minimum load condition σ^-

Calculate each bond stretch
$$s^-_{(k)(j)}$$

$N = N + 1$

Calculate the cyclic bond strain of each bond at the Nth load cycle
$$\varepsilon^N_{(k)(j)} = \left| s^+_{(k)(j)} - s^-_{(k)(j)} \right|$$

The bond is in the crack tip areas — False / True

Calculate the remaining life of bonds without the crack tip areas at the Nth load cycle
$$\lambda^N_{(k)(j)} = \lambda^N_{(k)(j)} - A_1 \left(\varepsilon^N_{(k)(j)} \right)^{m_1}$$

Calculate the remaining life of bonds within the crack tip areas at the Nth load cycle
$$\lambda^N_{(k)(j)} = \lambda^N_{(k)(j)} - A_2 \left(\varepsilon^N_{(k)(j)} \right)^{m_2}$$

$$\lambda^N_{(k)(j)} \le 0$$
or
$$s^+_{(k)(j)} \le s_0$$
False / True

New bond breakage

Fracture — False / True — END

Figure 5.13. Flowchart for simulation of fatigue crack growth

The numerical procedure for simulating crack growth is described as

1) Create a model

   Firstly, it is necessary to discretize a geometry of model into material points for the peridynamic calculation. Also, peridynamic parameters for the peridynamic calculation should be identified based on material properties, such as bond constant, critical bond stretch and peridynamic fatigue parameters.

2) Assign the initial remaining life

   All bonds in a material have an initial value of remaining life at the initial state before applying cycle loads (Eq. (4.1b)).

3) Define crack tip areas

   In order to distinguish bonds near crack tips from other bonds located far from the crack tips, it is essential to define the crack tip areas. Firstly, the crack at the Nth load cycle is defined in material points as [39]

$$\varphi_{(k)}^{N} \geq 0.35 \tag{5.20}$$

   where $\varphi_{(k)}^{N}$ is the local damage of material point k at the Nth load cycle. Any material points with the local damage $\varphi_{(k)}^{N} \geq 0.35$ is considered as the crack. Fig. 5.14 shows some kind of crack tip areas in the material, which the boundary radius of crack tip areas is typically defined as the horizon δ [13].
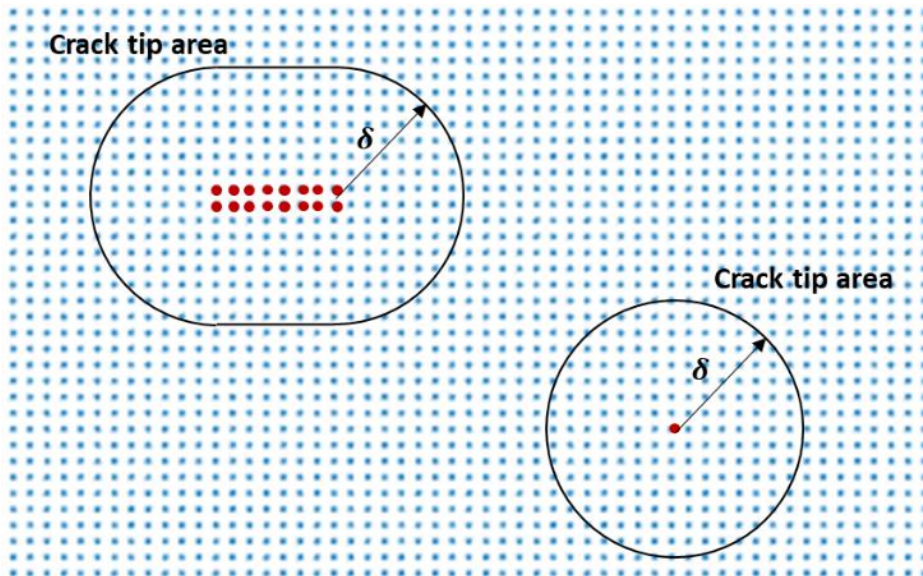
Figure 5.14. Cracks and crack tip area defined in material points (red points · is material points with local damage $\varphi_{(k)}^N \geq 0.35$)

4) Identify extreme loads of the Nth load cycle

In order to calculate the fatigue damage during the Nth load cycle, it is necessary to identify two extremes in the Nth load cycle. Fig. 5.4 shows the maximum and minimum points in each load cycle, which the only two extremes are required to calculate the Nth cyclic bond strain in the Nth load cycle.

5) Compute two static solutions under each extreme load condition

Peridynamic static solutions under each extreme load condition can be calculated by the direct solution as described in Chapter 5.1.

6) Calculate the cyclic bond strain of each bond at the Nth load cycle

The maximum and minimum bond stretches $s_{(k)(j)}^+$ and $s_{(k)(j)}^-$ of between material points k and j at the Nth load cycle can be calculated respectively based on the peridynamic static solutions. With the maximum and minimum bond stretches, the cyclic bond strain of each bond at the Nth load cycle can be calculated from Eq. (4.2).

7) Calculate the remaining life of each bond at the Nth load cycle

The remaining life of each bond at the Nth load cycle can be calculated by integrating Eq. (4.12) as below

$$\int_{\lambda_{(k)(j)}^{N-1}}^{\lambda_{(k)(j)}^{N}} d\lambda_{(k)(j)} = \int_{N-1}^{N} -A_2\left(\varepsilon_{(k)(j)}^{N}\right)^{m_2} dN \tag{5.21a}$$

and

$$\lambda_{(k)(j)}^{N} = \lambda_{(k)(j)}^{N-1} - A_2\left(\varepsilon_{(k)(j)}^{N}\right)^{m_2} \tag{5.21b}$$

where N is the number of cycles, $\lambda_{(k)(j)}^{N}$ is the remaining life of bond between material points k and j at the Nth load cycle, $\varepsilon_{(k)(j)}^{N}$ is the cyclic bond strain between material points k and j at the Nth load cycle, A_2 and m_2 are the peridynamic fatigue parameters.

The bond breakage occurs when

$$\lambda_{(k)(j)}^{N} \leq 0 \tag{5.22}$$

or

$$s_{(k)(j)}^{+} \geq s_0 \tag{5.23}$$

where s_0 is the critical bond stretch for failure under static loading.

8) Fracture

By cyclic loadings, multiple new bond breakages occur, which cause the crack growth. Finally, when the crack growth reaches surfaces of the material or the material is totally divided into two materials, the final fracture occurs, and the simulation is ends.

5.3.3 Peridynamic simulation for crack growth

A discretization of two-dimensional model is represented in Fig. 5.15, which the R_b indicates volume of boundary layers applied body forces. Peridynamic parameters are represented as

- Total number of material points: 15100
- Spacing between material points: $\Delta = 0.5$ mm
- Initial length of the pre-existing crack: $a = 12.5$ mm
- Thickness: $t = 6.11$ mm
- Horizon: $3.015 \times \Delta = 1.5075$ mm
- Critical bond stretch: $s_0 = 0.01$
- Static solution: Direct solution
- Incremental volume of material points: $\Delta V = t \times \Delta \times \Delta = 1.5275$ mm^3
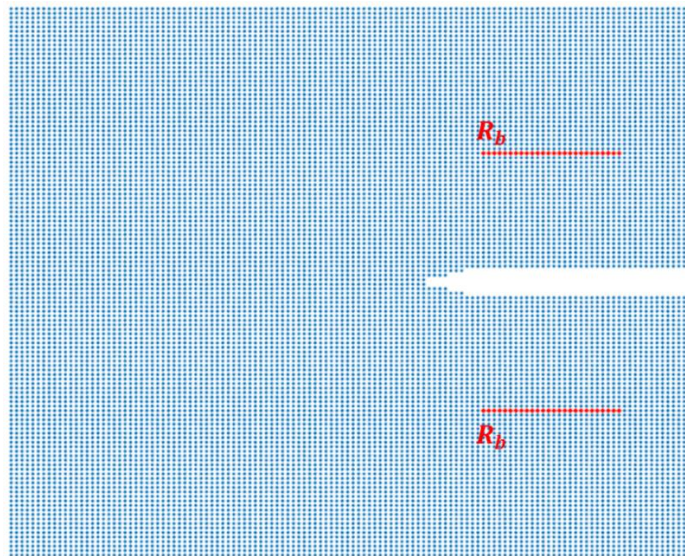
Figure 5.15. Geometry of numerical model for fatigue crack growth and its discretization

5.3.3.1 Calibration of peridynamic fatigue parameters for crack growth

The fatigue crack growth rate of common metallic materials is largely influenced by material microstructure, thickness of component, and load ratio [40]. The fatigue crack growth of 7075-T651 aluminium alloy is also greatly influenced by load ratio. Considering the load ratio effect on the fatigue crack growth rate, Kujawski [41] proposed the modified Paris law as

$$\frac{da}{dN} = C'(K^*)^{M'} \tag{5.24a}$$

and

$$K^* = (K_{max})^{\gamma}(\Delta K^+)^{1-\gamma} \tag{5.24b}$$

where C', M' and γ are the material fatigue constants calibrated by fatigue tests, K_{max} is the maximum stress intensity factor in a loading cycle, ΔK^+ is the positive part of the range of the stress intensity factor in a loading cycle. These parameters K_{max} and ΔK^+ are represented in Fig. 5.16.
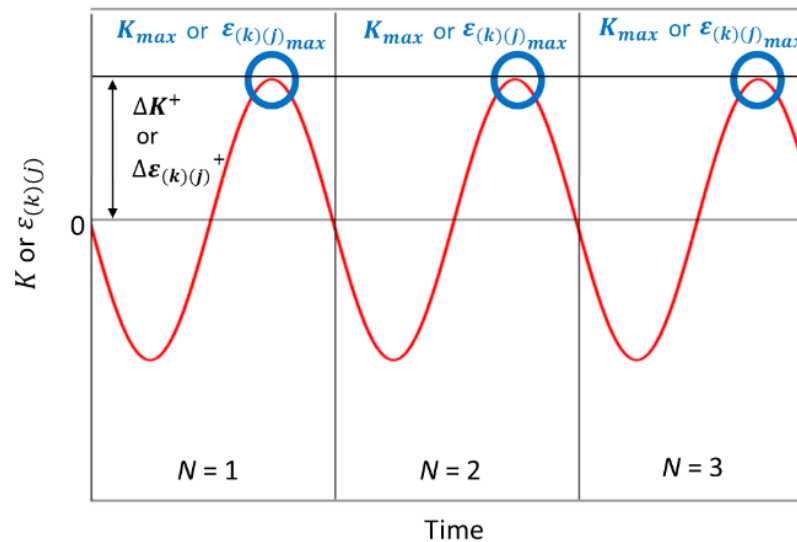
Figure 5.16. Representation of ΔK^+, K_{max}, $\varepsilon_{(k)(j)_{max}}$ and $\Delta\varepsilon_{(k)(j)}{}^+$ in each load cycle

To consider the load ratio effect in the peridynamic fatigue model, Silling and Askari [13] modified Eq. (4.12) by assuming that bond strains near crack tips are proportional to the stress intensity factor, which is given as below [13]

$$\frac{d\lambda_{(k)(j)}}{dN} = -A_2\left(\varepsilon_{(k)(j)}{}^*\right)^{m_2} \tag{5.25a}$$

and

$$\varepsilon_{(k)(j)}{}^* = \left(\varepsilon_{(k)(j)_{max}}\right)^{\gamma}\left(\Delta\varepsilon_{(k)(j)}{}^+\right)^{1-\gamma} \tag{5.25b}$$

where γ is the fatigue constant in Eq. (5.24b), $\varepsilon_{(k)(j)_{max}}$ is the maximum cyclic bond strain between material points k and j at each cycle, and $\Delta\varepsilon_{(k)(j)}{}^+$ is the positive part of the range of cyclic bond strain between material points k and j at each cycle. These parameters $\varepsilon_{(k)(j)_{max}}$ and $\Delta\varepsilon_{(k)(j)}{}^+$ are represented in Fig. 5.16.

To calibrate the peridynamic fatigue parameters A_2 and m_2, experimental data [40] are used to describe the Paris curve of 7075-T651 aluminium alloy. In this study, the modified Paris curve (Eq. (5.24)) is used to consider the load ratio effect. The fatigue constants of 7075-T651 aluminium alloy for Eq. (5.24) are represented in Table 5.4. In this case, the fatigue constants of modified Paris raw can be easily obtained from the material properties in Table 5.4. If there were no the fatigue constants of modified Paris raw, it is possible to calculate the fatigue constants from the crack growth test data for a material. A process of the calculation for the fatigue parameters C', M' and γ are described in Chapter 6.1.1.

Table 5.4. Fatigue constants of 7075-T651 aluminium alloy [40]

C'	6.0×10^{-8}
M'	3.32
γ	0.35

The crack growth rate of the ASTM E647 standard compact specimen can be calculated in the analytical way based on Eq. (5.24), which the stress intensity factor of the ASTM E647 standard compact specimen can be calculated by an equation as [40]

$$K = \frac{P(2 + \frac{a}{W})}{B\sqrt{W}\left(1 - \frac{a}{W}\right)^{3/2}}\left(0.886 + 4.64\left(\frac{a}{W}\right) - 13.32\left(\frac{a}{W}\right)^2 + 14.72\left(\frac{a}{W}\right)^3 - 5.6\left(\frac{a}{W}\right)^4\right) \quad (5.26)$$

where P is the applied force, B is the thickness of the compact specimen, W is the distance between the right edge of the specimen and the vertical line of the applied force P, and a is the length of crack measured from the line of the applied force P. Fig. 5.17 shows the ASTM E647 standard compact specimen.
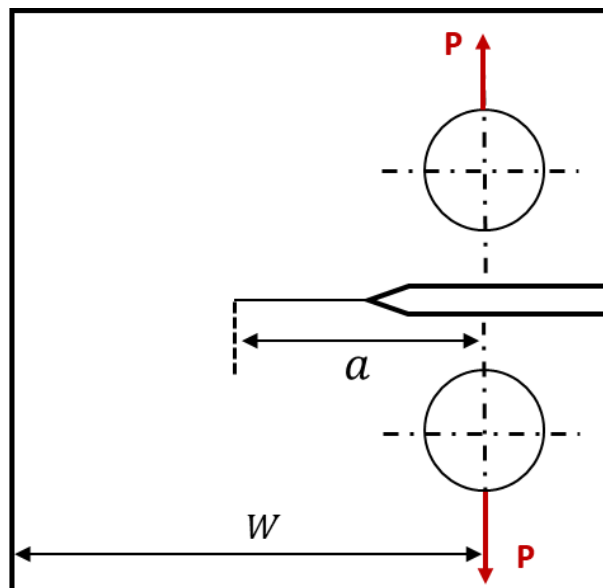
Figure 5.17. ASTM E647 standard compact specimen

The peridynamic fatigue parameter m_2 can be determined by the fatigue constant M' in Eq. (4.25). The numerical procedure to calibrate peridynamic fatigue parameter A_2 in Eq. (4.12) is described in Fig. 5.18.
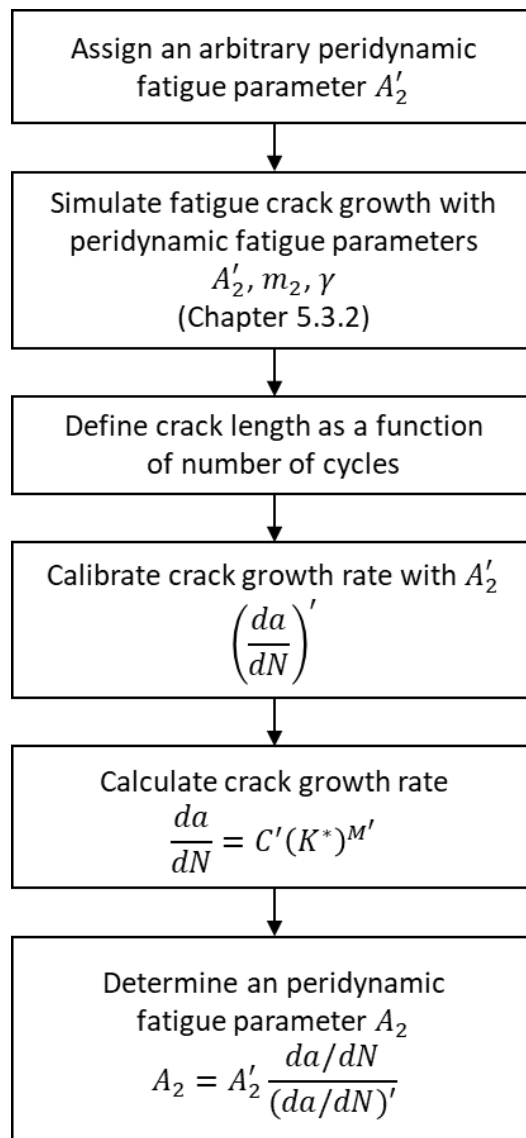
Figure 5.18. Flowchart for calibration of peridynamic fatigue parameter A_2

The numerical procedure for calibrating the peridynamic fatigue parameter A_2 is described as

1) Assign an arbitrary peridynamic fatigue parameter A_2'

   To determine the peridynamic fatigue parameters A_2, it is necessary to assign an arbitrary peridynamic fatigue parameter A_2'. In this study, the arbitrary peridynamic fatigue parameter A_2' is defined as

$$A_2' = 10,000 \tag{5.39}$$

2) Simulate fatigue crack growth with A_2'

   To calculate crack growth rate of A_2', A peridynamic simulation is performed with peridynamic fatigue parameters A_2', m_2 and γ with the simulation procedure for fatigue crack growth as described in Chapter 5.3.2.

3) Define crack length as a function of number of cycles

   The crack length can be represented as a function of number of cycles from peridynamic results. Fig. 5.19 shows crack length versus number of cycles.
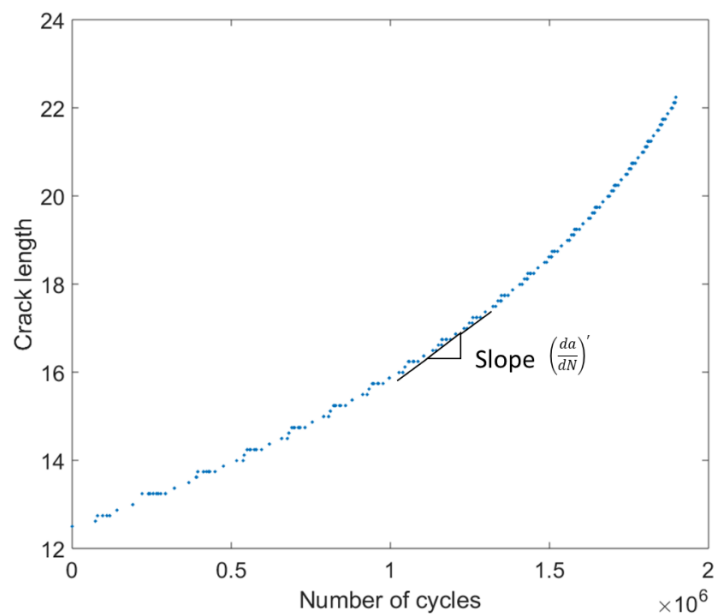
Figure 5.19. Crack-Cycle curve of peridynamic simulation by using A_2'

4) Calibrate crack growth rate $\left(\frac{da}{dN}\right)'$

The crack growth rate $\left(\frac{da}{dN}\right)'$ can be calibrated by slopes of the Crack-Cycle curve as shown in Fig. 5.19. The crack growth rate $\left(\frac{da}{dN}\right)'$ with respect to crack length is represented in Fig. 5.20.

5) Calculate crack growth rate $\frac{da}{dN}$

Authentic crack growth rate $\frac{da}{dN}$ can be obtained from the fatigue test results of Zhao and Jiang [40]. The crack growth rate $\frac{da}{dN}$ with respect to crack length is represented in Fig. 5.20.

6) Determine an authentic peridynamic fatigue parameter A_2

The peridynamic fatigue parameter A_2 can be calculated by Eq. (4.28). Fig. 5.21 shows results of calculation. Finally, a mean value of A_2 in the Fig. 5.21 is determined as a final peridynamic fatigue parameters A_2. After determining the peridynamic fatigue parameter A_2, Eq. (4.20) will be used for crack growth simulation. The resulting peridynamic fatigue parameters for crack growth phase are represented in Fig. 5.22 and Table 5.5.
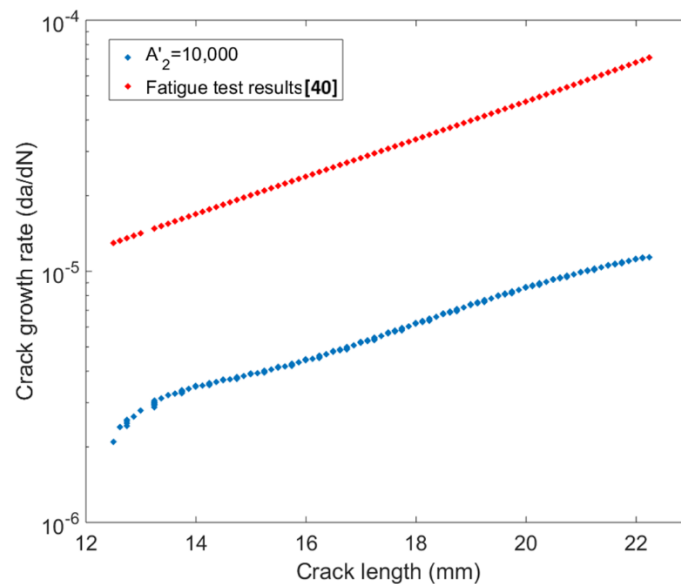
Figure 5.20. Crack growth rate $\frac{da}{dN}$ and $\left(\frac{da}{dN}\right)'$ with respect to crack length
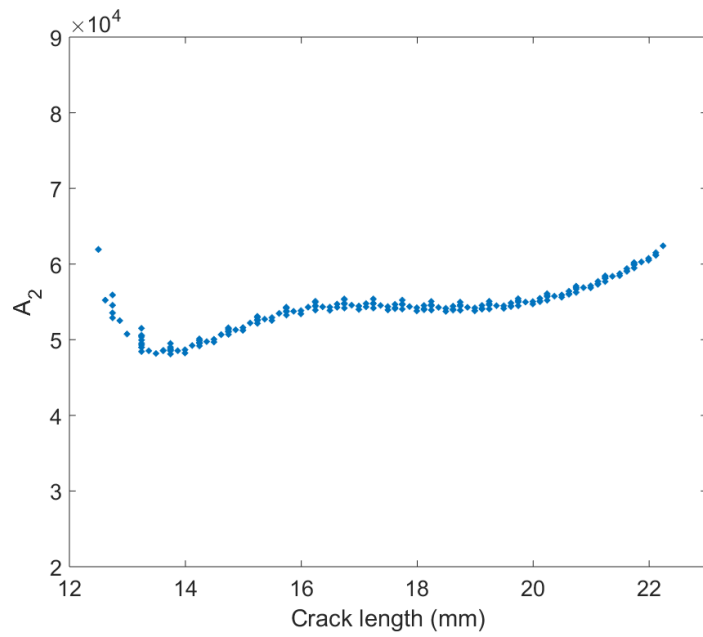
Figure 5.21. Calculated peridynamic fatigue parameter A_2 with respect to crack length
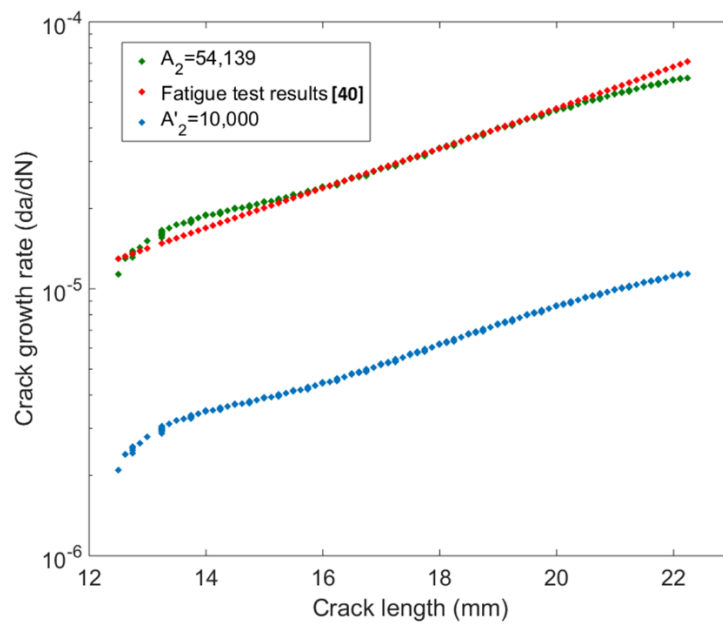
Figure 5.22. Crack growth rate of $A_2 = 54{,}139$ with respect to crack length

Table 5.5. Peridynamic fatigue parameters for crack growth of 7075-T651

A_2	54138.96
m_2	3.32
γ [41]	0.35

5.3.4 Numerical results and validation

To validate peridynamic static solutions, first a peridynamic static solution is compared with FEM by using ANSYS software. In FEM, a plane stress element with thickness is used.

Fig. 5.23 and 5.24 show comparison between the peridynamic static solution and the FEM static solution under a uniaxial tension in opposite directions at two pins of top and bottom with forces $P^+ = 1500$ N. These results show that the peridynamic static solution has similar displacement distributions with the FEM static solution.
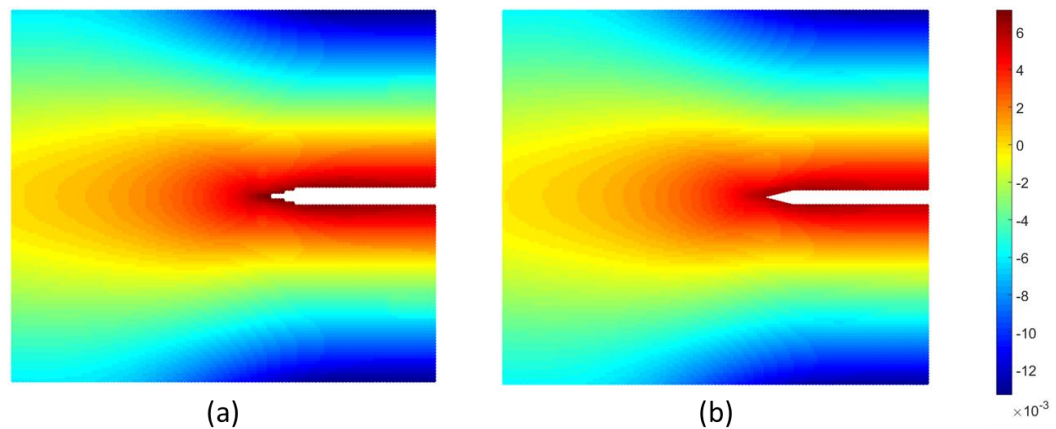
Figure 5.23. Displacement distribution in x-direction under uniaxial tension in opposite directions at two pins of top and bottom with forces $P^+ = 1500\,N$, (a) peridynamic static solution (b) FEM static solution
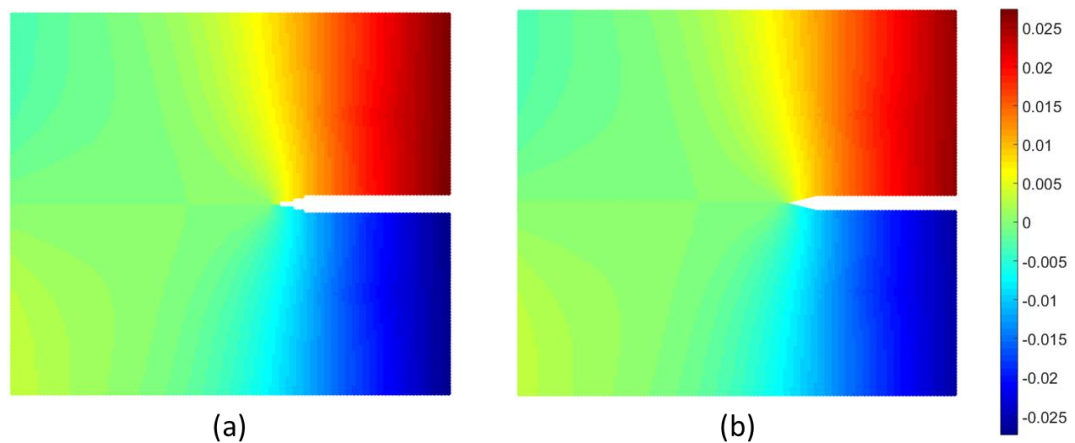
Figure 5.24. Displacement distribution in y-direction under uniaxial tension in opposite directions at two pins of top and bottom with forces $P^+ = 1500\,N$, (a) peridynamic static solution (b) FEM static solution

After verifying the peridynamic results, a simulation of fatigue crack growth is performed with the simulation procedure of crack growth described in Chapter 5.3.2. The fatigue crack growth is demonstrated in Fig. 5.25, which the fatigue damage is represented in the local damage (Eq. (3.6)). The numerical result of fatigue crack growth is represented and compared with the fatigue test results of Zhao and Jiang [40] in Fig. 5.26.
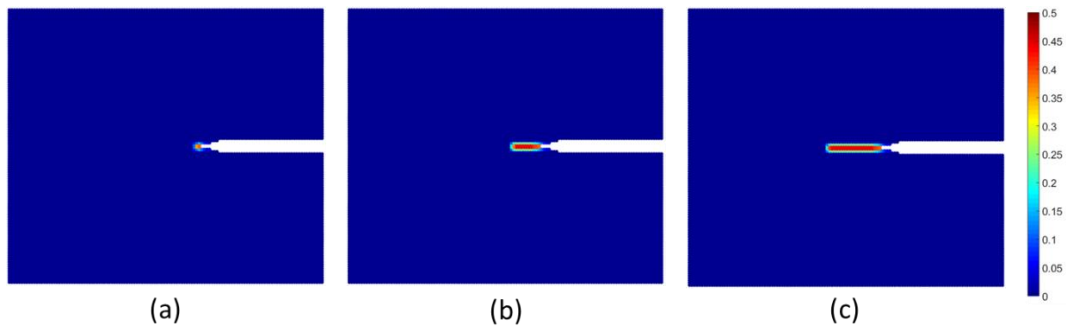
Figure 5.25. Fatigue damage of numerical results, (a) $N = 0$ and crack length is 12.5 mm, (b) $N = 233706$ and crack length is 17.24 mm, (c) $N = 352196$ and crack length is 22.24 mm
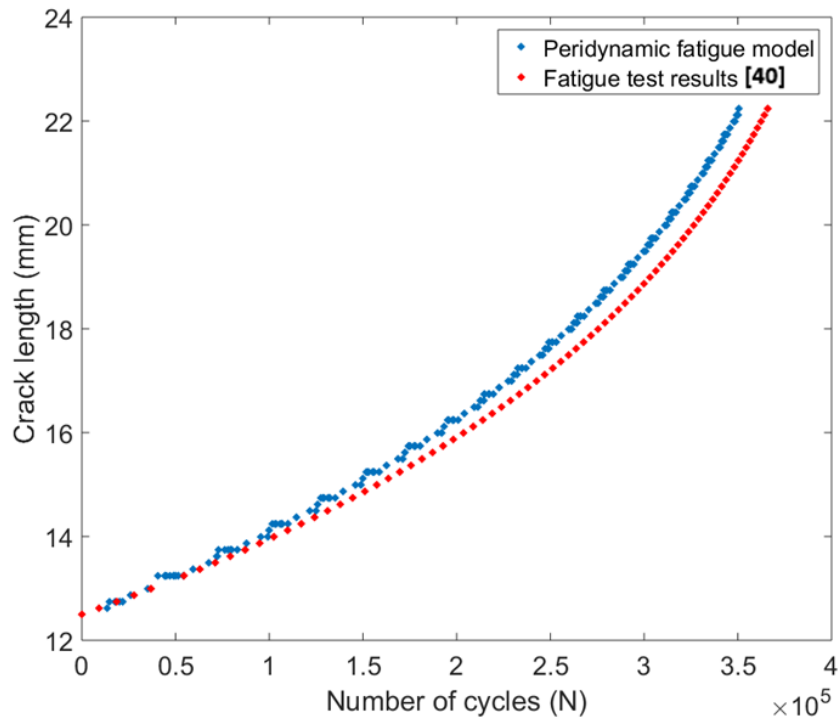
(a)
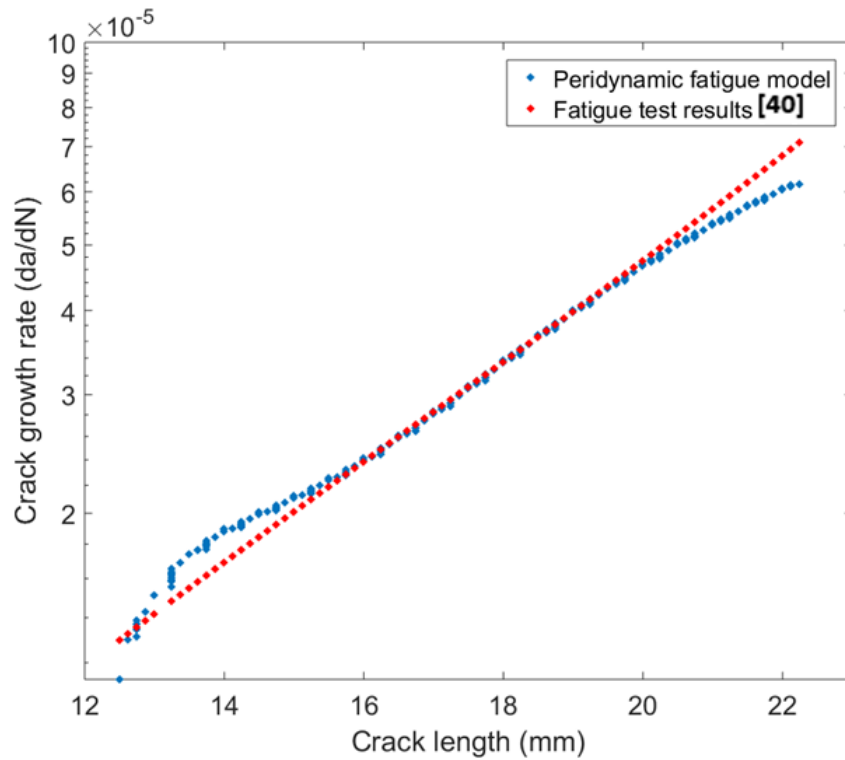
(b)

Figure 5.26. Numerical results of peridynamic calculation with peridynamic fatigue parameter A_2 and fatigue test results of Zhao and Jiang [40], (a) crack length as a function of number of cycles, (b) crack growth rate as a function of crack length

5.4 Conclusion

In this chapter, two phases of fatigue failure are simulated with the peridynamic fatigue model. One is the fatigue tensile test for the crack nucleation and the other is the compact test for the crack growth.

In the fatigue tensile test, the numerical results show that the crack nucleation occurs where the stress is concentrated, and the fatigue damage is developed based on the crack nucleation. Also, comparing the numerical results with the fatigue test results of Zhao and Jiang [38], it is seen that the peridynamic fatigue model is capable of predicting the fatigue crack nucleation. The Fig. 5.8 show that the occurrence of first bond breakage at the various bond cyclic strain is matched with the fatigue results of Zhao and Jiang [38].

In the compact test, the numerical result shows that the peridynamic fatigue model is capable of predicting the fatigue crack growth. The results of crack length and the crack growth rate from the numerical test are matched with the fatigue results of Zhao and Jiang [40]. However, it is seen that errors between the numerical results and the fatigue results of Zhao and Jiang [40] increase as the crack length increases. The reason for the errors are considered that all material behaviours in peridynamic calculations are assumed as the linear elastic material behaviour. 7075-T651 aluminium alloy is a ductile material which shows the nonlinear plastic material behaviour near the crack tip.

6. FATIGUE ASSESSMENT OF FILLET WELDED JOINTS

In this section, a new computational approach to fatigue assessment of fillet welded joints is demonstrated. The effect of unwelded zone in fillet welded joints is investigated by estimating the fatigue performance with respect to the length of unwelded zone. Fatigue failures by crack growth and the path of crack growth in fillet welded joints are simulated by using the peridynamic fatigue model. It is assumed that all material behaviour in peridynamic calculations are linear elastic.

6.1 Numerical model for fillet welded joint

A two-dimensional numerical model for fatigue assessment of fillet welded joints is shown in Fig. 6.1, where $2a$ represents the length of unwelded zone. Two different materials are used in this numerical model. The SWS 490B mild carbon steel is used as a material of main member and the AWS A5.18 ER70S-6 is used as a material of weld metal. The model is subjected to cyclic loading at the top and it is fixed at the bottom. Loading and weld geometry conditions of all cases for fatigue assessment are described in Table 6.1.

Boundary conditions:
- $u_y = 0$ at $y = 0$
- $u_x = 0$ at $y = 0$ and $x = 0$

Loading conditions: Uniaxial cyclic loading σ (MPa) at $y = 26\ mm$
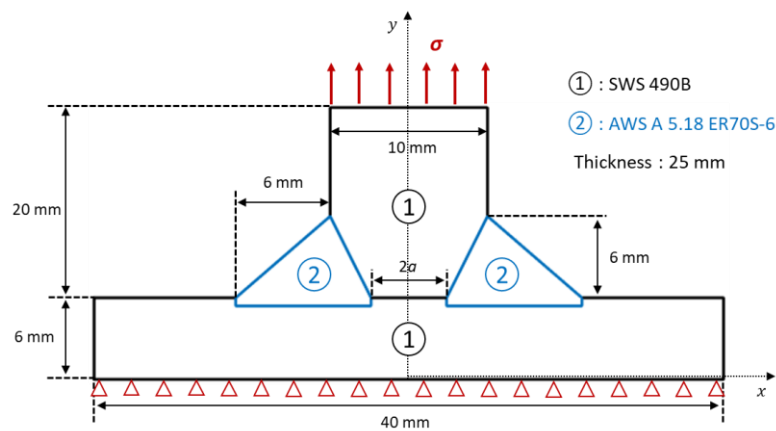
Figure 6.1. Geometry of a fillet welded joint under uniaxial cyclic loading

Table 6.1. Loading conditions for fatigue assessment of fillet welded joints

Case	Length of unwelded zone (2a) (mm)	Stress amplitude (MPa)	Mean stress (MPa)	Load ratio	Frequency (Hz)
1	2.4	60	60	0	10
2	2.4	70	70	0	10
3	2.4	80	80	0	10
4	2.4	90	90	0	10
5	2.4	100	100	0	10
6	4.8	60	60	0	10
7	4.8	70	70	0	10
8	4.8	80	80	0	10
9	4.8	90	90	0	10
10	4.8	100	100	0	10
11	7.2	60	60	0	10
12	7.2	70	70	0	10
13	7.2	80	80	0	10
14	7.2	90	90	0	10
15	7.2	100	100	0	10

6.1.1 Material properties of numerical model

Mechanical properties of SWS 490B mild carbon steel and AWS a5.18 ER70S-6 are given in Table 6.2 and 6.3, respectively.

Table 6.2. Mechanical properties of SWS 490B mild carbon steel [42]

Elasticity modulus, E	200 GPa
Poisson's ratio, v	0.33
Yield stress, σ_Y	368 MPa
Ultimate strength, σ_u	529 MPa
Elongation	23.0 %

Table 6.3. Mechanical properties of AWS A5.18 ER70S-6 [43]

Elasticity modulus, E	250 GPa
Poisson's ratio, v	0.33
Yield stress, σ_Y	360 MPa
Ultimate strength, σ_u	485 MPa
Elongation	26.0 %

For the material of AWS A5.18 ER70S-6, there are no the fatigue constants of modified Paris raw. Therefore, the fatigue constants C', M' and γ are calculated directly in this thesis. Fatigue constants for AWS A5.18 ER70S-6 are calibrated by using fatigue test results of DeMarte [43]. To calibrate the fatigue constants of modified Paris law C', M' and γ, fatigue test results performed under at least two different load ratio conditions are necessary. The fatigue test results of DeMarte [43] are represented in Fig. 6.2, which is the results of two different load ratio $R_1 = 0.05$ and $R_2 = 0.6$.
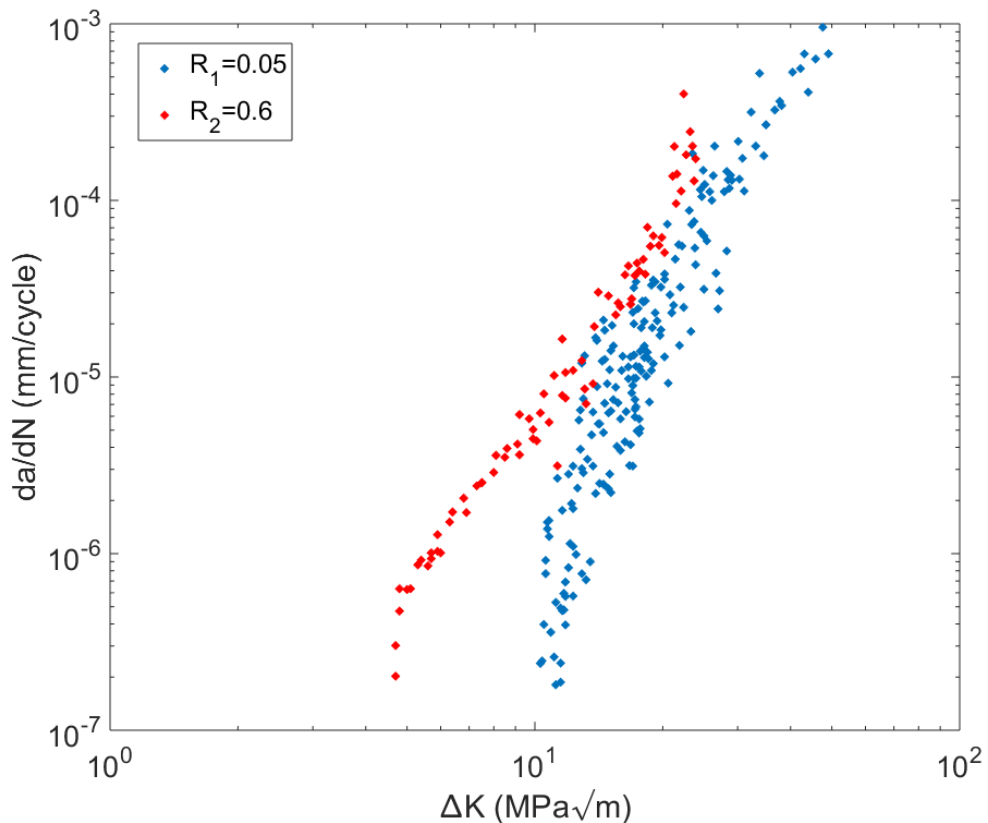
Figure 6.2. Fatigue crack growth test results of DeMarte [43]

To consider the influence of load ratio, it is necessary for all test results of DeMarte [43] to be converted and expressed into the modified Paris curve of Eq. (5.24). The fatigue constant γ in Eq. (5.24b) is determined by the following relation [41]

$$\gamma = \frac{log(\Delta K_1^+/\Delta K_2^+)}{log\left(\dfrac{1-R_1}{1-R_2}\right)} \tag{6.1}$$

where R is the load ratio, and ΔK^+ is the positive part of the range of the applied stress intensity factor represented in Fig. 5.16.

Fig. 6.3 shows calibration for ΔK_1^+ and ΔK_2^+ of test results of DeMarte [43]. The fatigue constant γ with respect to the crack growth rate can be calculated from Eq. (6.1). Fig. 6.4 shows a final fatigue constant γ is determined as a mean value of γ.

The modified Paris curve of AWS A5.18 ER70S-6 of Eq. (5.24) is represented in Fig. 6.5. The fatigue constants of the AWS A5.18 ER70S-6 are represented in Table 6.4.
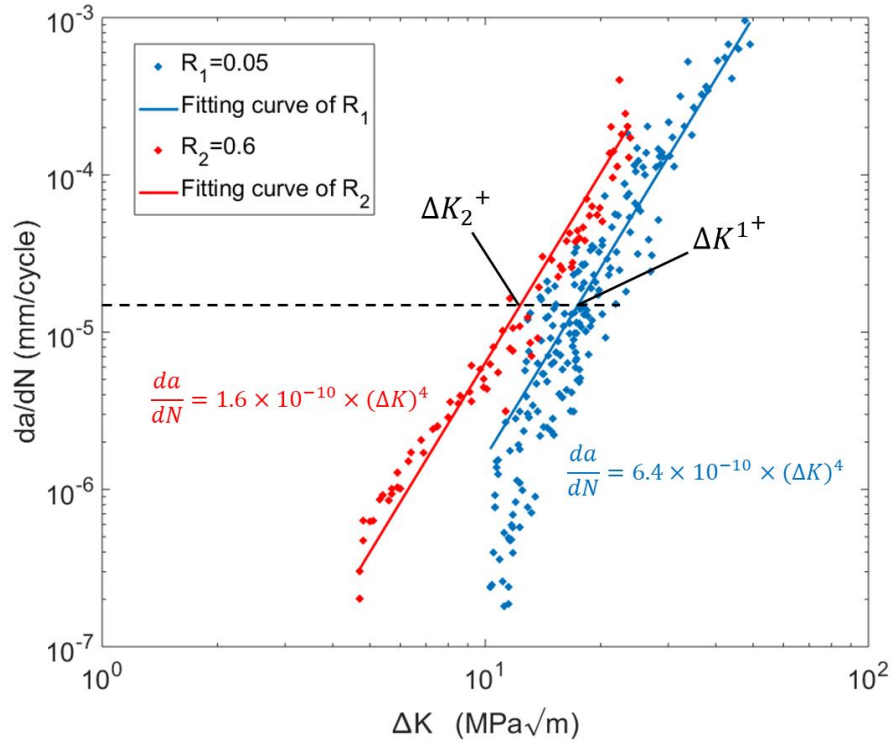
Figure 6.3. Calibration of ΔK_1^+ and ΔK_2^+ from test results of DeMarte [43]
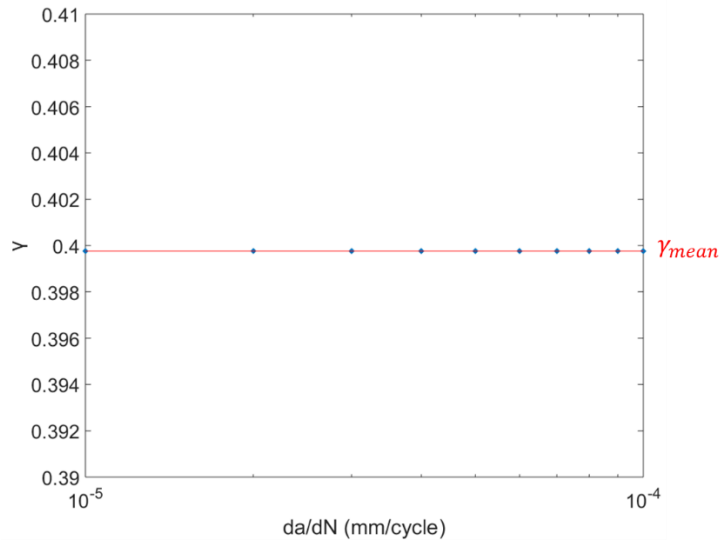
Figure 6.4. Values of fatigue constant γ with respect to crack growth rate and mean value
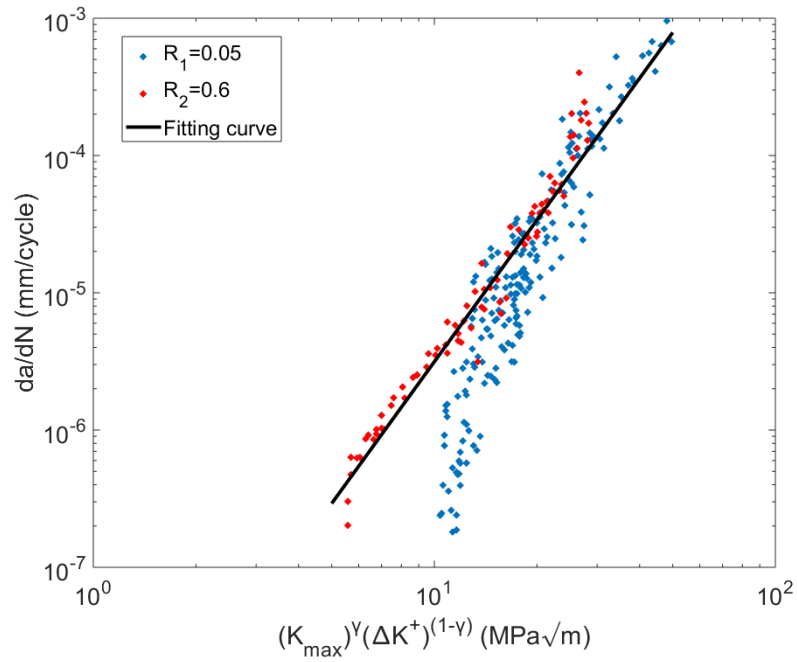
Figure 6.5. Modified fatigue crack growth data by using test results of DeMarte [43]

Table 6.4. Fatigue constants of AWS A5.18 ER70S-6

C'	1.167×10^{-9}
M'	3.43
γ	0.3998

6.2 Peridynamic simulation for fillet welded joint

The discretization of two-dimensional fillet welded joint numerical model is shown in Fig. 6.6. In this figure, R_b indicates material points to apply body forces and R_c indicates material points for boundary conditions. Peridynamic parameters are described as

- Total number of material points: 12530

- Spacing between material points: $\Delta = 0.2$ mm

- Thickness: $t = 25$ mm

- Horizon: $3.015 \times \Delta = 0.603$ mm

- Critical bond stretch of the material ①: $s_{1_0} = 0.0113$

- Critical bond stretch of the material ②: $s_{2_0} = 0.0091$

- Static solution: Direct static solution

- Incremental volume of material points: $\Delta V = t \times \Delta \times \Delta = 1$ mm^3

① : SWS 490B

② : AWS A 5.18 ER70S-6
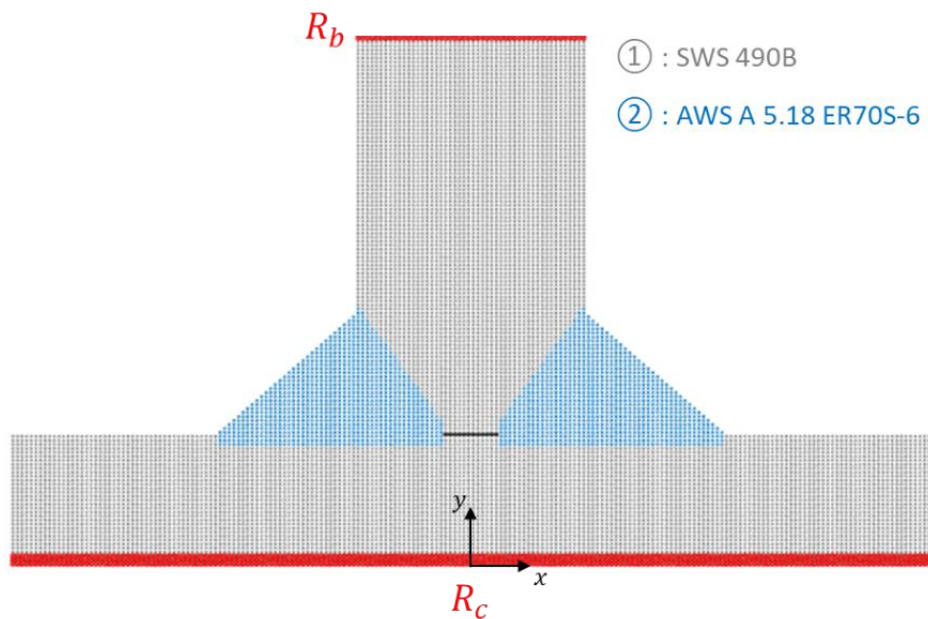
Figure 6.6. Geometry of fillet welded joint and its discretization

The peridynamic model is comprised of two different materials, which one is for main members and the other is for the weld metal. Material points near interfaces between materials of the main member and the weld metal are required to be corrected by surface effects [33]. The bond constant of each material is achieved by integrating strain energy density at each material point within the horizon [33]. However, material points near material interfaces include material points of the other material within their horizon. A material point $\mathbf{x}_{(i)}$ interacting with material points $\mathbf{x}_{(j)}$ and $\mathbf{x}_{(m)}$ is shown in Fig. 6.7. The bond constant between material points $\mathbf{x}_{(i)}$ and $\mathbf{x}_{(j)}$ is $c_{(i)(j)}$ is different from the bond constant $c_{(i)(m)}$ between material points $\mathbf{x}_{(i)}$ and $\mathbf{x}_{(m)}$, because the material points $\mathbf{x}_{(i)}$ and $\mathbf{x}_{(m)}$ are embedded in two different materials. The bond constant $c_{(i)(m)}$ can be expressed as [44]

$$c_{(i)(m)} = \frac{l_1 + l_2}{\dfrac{l_1}{c_1} + \dfrac{l_2}{c_2}} \tag{6.2}$$

where l_1 is the segment of the distance between material points $\mathbf{x}_{(i)}$ and $\mathbf{x}_{(m)}$ in material 1, l_2 is the segment of the distance between material points $\mathbf{x}_{(i)}$ and $\mathbf{x}_{(m)}$ in material 2, c_1 is the bond constant of material 1, and c_2 is the bond constant of material 2.
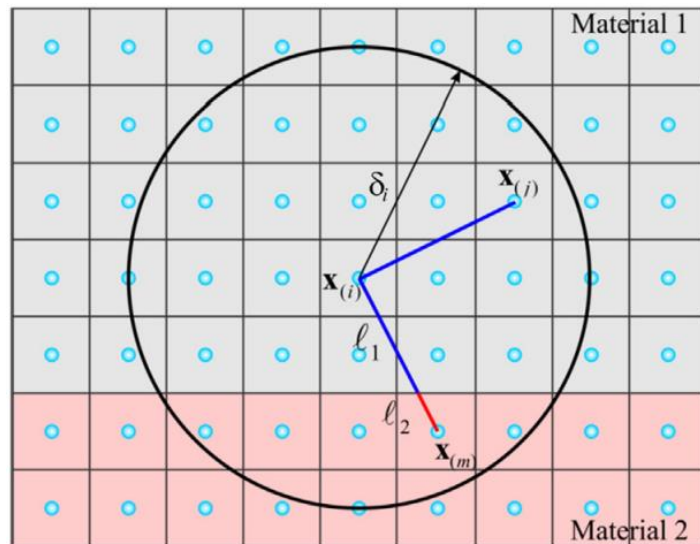
Figure 6.7. Interactions of material point $\pmb{x}_{(i)}$ with material points $\pmb{x}_{(j)}$ and $\pmb{x}_{(m)}$ [44]

6.2.1 Calibration of peridynamic fatigue parameters

It is necessary to calibrate peridynamic fatigue parameters for the simulation of fatigue crack growth in the fillet welded joint. The fillet welded joint involves an unwelded zone, which is considered as a pre-existing crack in the material. Therefore, the only peridynamic fatigue parameters A_2 and m_2 of crack growth phase are necessary.

The peridynamic fatigue parameter m_2 can be obtained easily from Eq. (4.25). For the peridynamic fatigue parameter A_2, a simulation of fatigue crack growth is performed with a two-dimensional numerical model, which is represented in Fig. 6.8. Two materials are used in the numerical model. One is the ASTM A36 as a main material and the other is the AWS A5.18 ER70S-6 as a weld material. Mechanical properties of ASTM A36 are given in Table 6.5. The fatigue crack growth in the specimen is demonstrated in Fig. 6.9, and the result of simulation is compared with the fatigue test results of DeMarte [43] in Fig. 6.10. The resulting peridynamic fatigue parameters of AWS A5.18 ER70S-6 are represented in Table. 6.6.
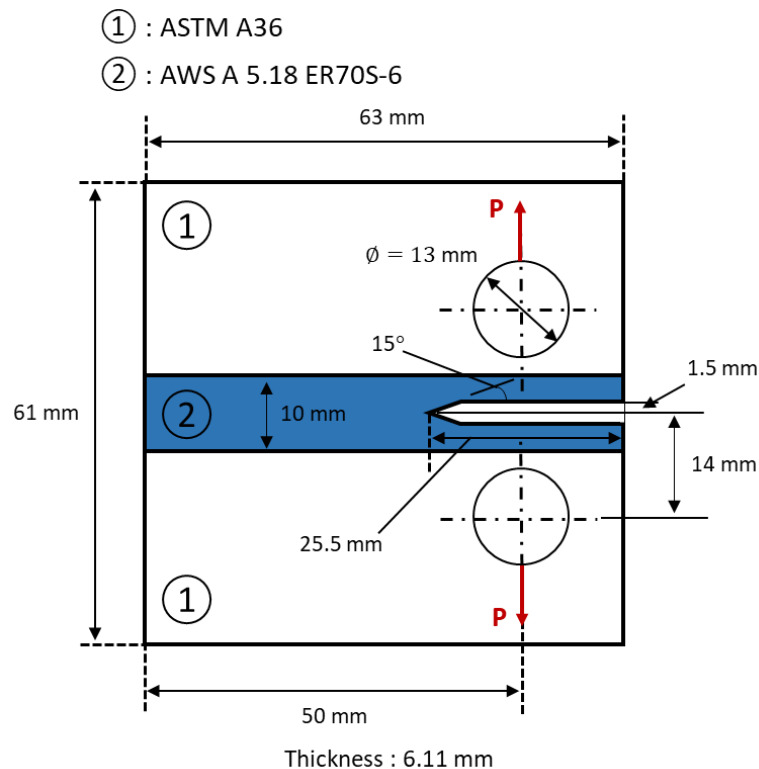
Figure 6.8. Numerical model for calibration of peridynamic fatigue parameter A_2

Table 6.5. Mechanical properties of ASTM A36 [43]

Elasticity modulus, E	200 GPa
Poisson's ratio, ν	0.33
Yield stress, σ_Y	250 MPa
Ultimate strength, σ_u	400 MPa
Elongation	23.0 %
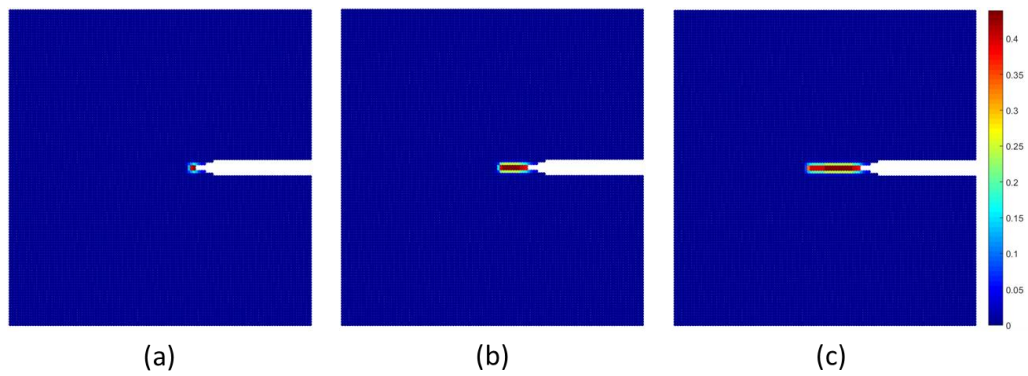
Figure 6.9. Fatigue damage of numerical results, (a) $N = 0$ and crack length is 12.5 mm, (b) $N = 114{,}915$ and crack length is 17.11 mm, (c) $N = 171{,}468$ and crack length is 22.11 mm

Table 6.6. Peridynamic fatigue parameters of AWS A5.18 ER70S-6

A_2	1.39×10^5
m_2	3.43
γ	0.3998
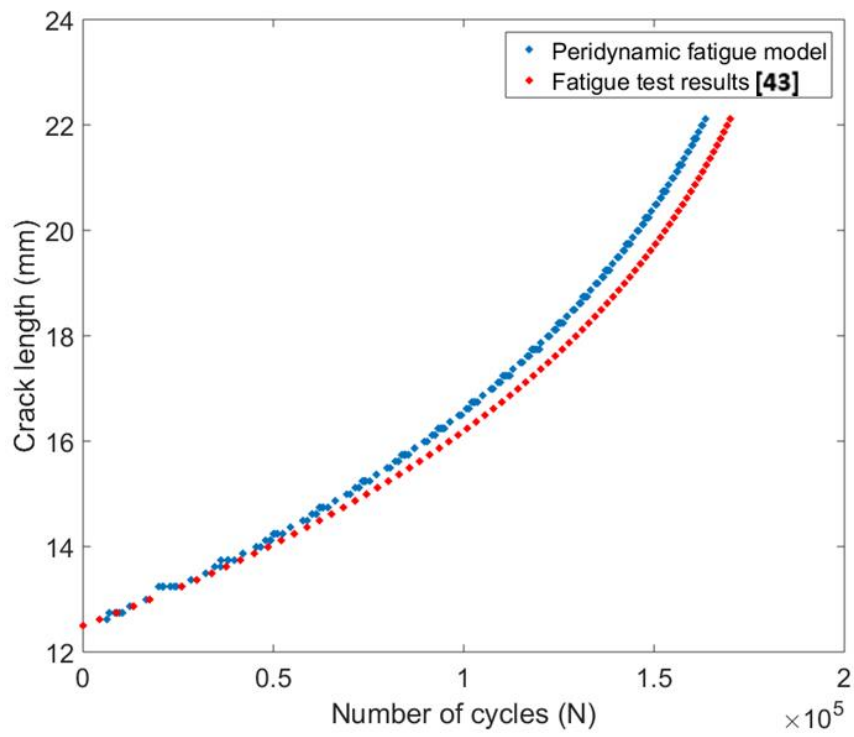
(a)
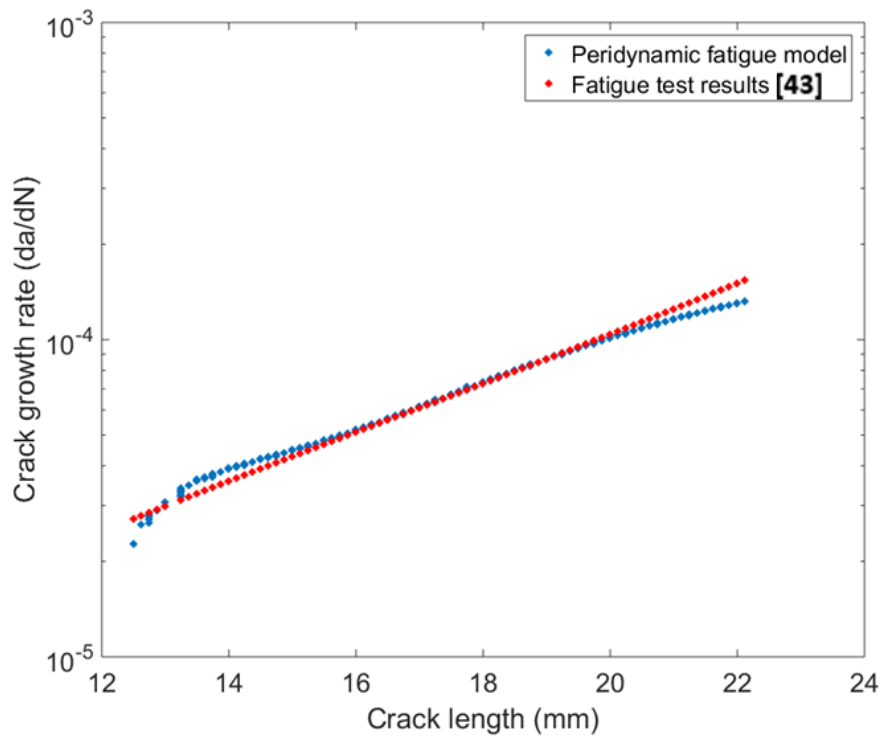
(b)

Figure 6.10. Numerical results of peridynamic calculation with peridynamic fatigue parameter A_2 and fatigue test results of DeMarte [43], (a) crack length as a function of number of cycles, (b) crack growth rate as a function of crack length

6.3 Numerical results and validation

To validate peridynamic static solutions, first a peridynamic static solution is compared with FEM by using ANSYS software. In FEM, a plane stress element with thickness is used.

Fig. 6.11 and 6.12 show comparison between the peridynamic static solution under a uniaxial tension loading at the top with forces $\sigma = 200$ MPa. These results show that the peridynamic static solution has similar displacement distributions with the FEM static solution.
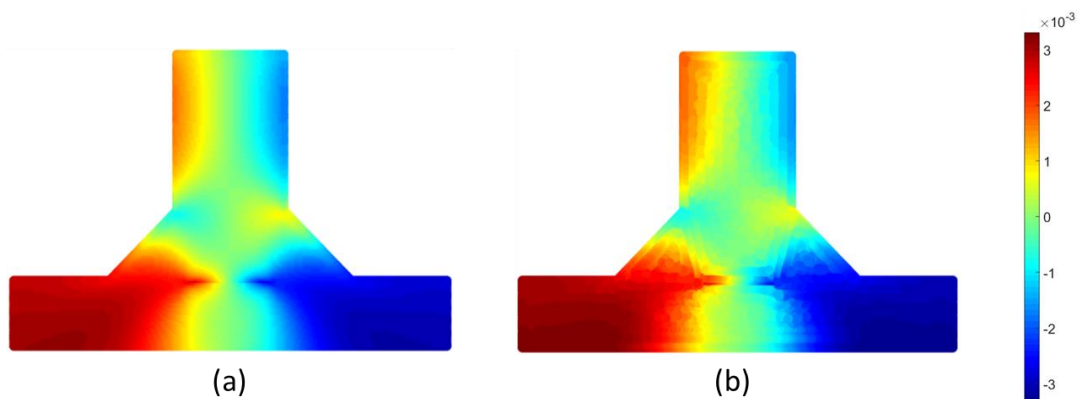
Figure 6.11. Displacement distribution in x-direction under a uniaxial tension loading at top with forces $\sigma = 200$ MPa, (a) peridynamics static solution (b) FEM static solution
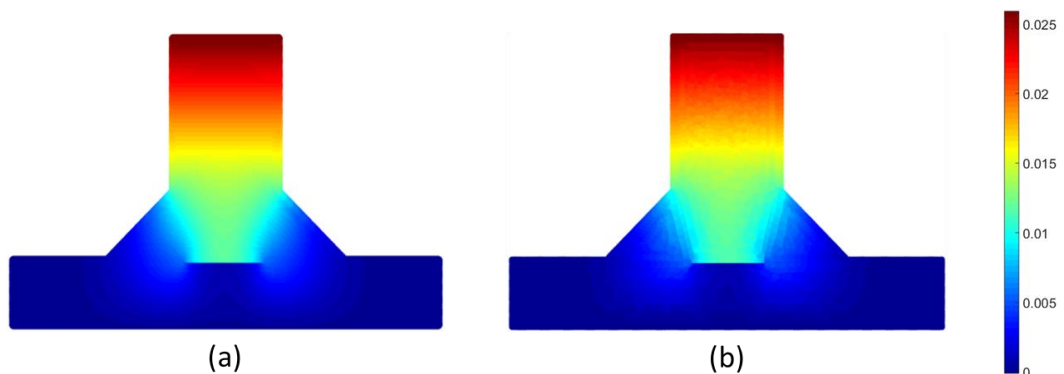
Figure 6.12. Displacement distribution in y-direction under a uniaxial tension loading at top with forces $\sigma = 200$ MPa, (a) peridynamics static solution (b) FEM static solution

After verifying the peridynamic results, peridynamic simulations for fatigue assessment of fillet welded joints are performed by using the simulation procedure provided in Fig. 5.13. The fatigue crack growth in the fillet welded joint is demonstrated in Fig. 6.13, 6.14, and 6.15, which show the fatigue crack growth in fillet welded joints according to the length of unwelded zones for different conditions. Crack patterns are different for different length of unwelded zone. However, the crack patterns are similar for same length of unwelded zone even for different loading conditions.

Numerical results of the peridynamic simulation are shown in Fig. 6.16. The numerical results are fatigue performances of fillet welded joints under different conditions as described in Table 6.1. In Fig. 6.16, the number of cycles is when the fillet welded joint model is totally divided into two materials.

Lee [45] investigated the characteristics of fatigue failure with respect to the length of unwelded zone. The fatigue tests were performed with the fillet welded joint specimen comprised of the SWS 490B welded with the weld wire of AWS A5.18 ER70S-6 by the GMAW welding method. To validate the numerical results, the results are compared with fatigue test results of Lee [45] as shown in Fig. 6.17 and 6.18.
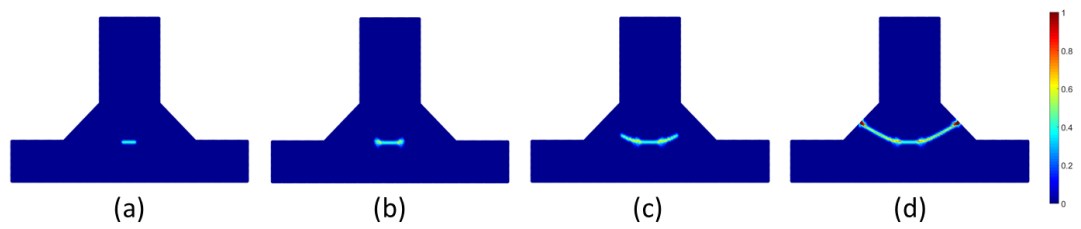
Figure 6.13. Fatigue damage in numerical model with the length of unwelded zone 2.4 mm for case 3 (a) $N = 0$ (b) $N = 481,468$ (c) $N = 674,095$ (d) $N = 699,623$
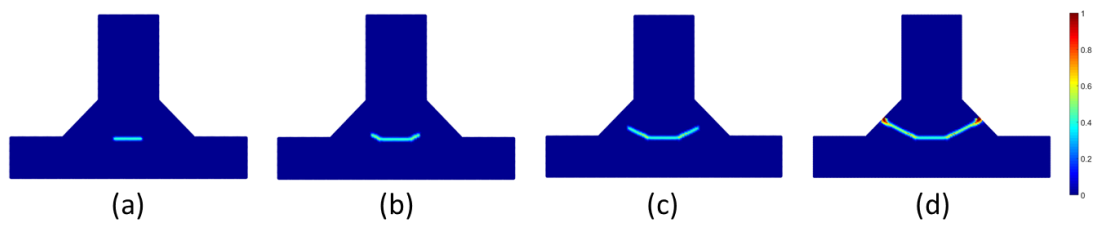
Figure 6.14. Fatigue damage in numerical model with the length of unwelded zone 4.8 mm for case 8, (a) $N = 0$ (b) $N = 183,637$ (c) $N = 227,882$ (d) $N = 233,606$
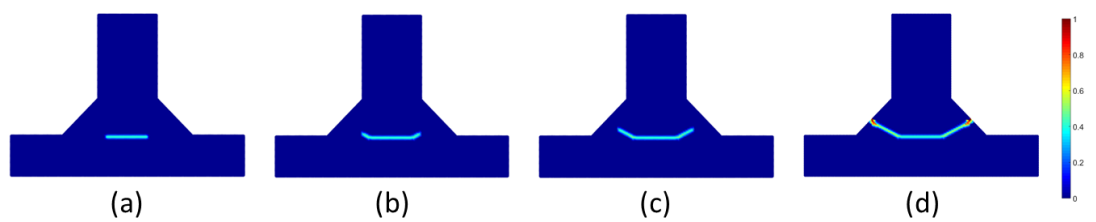
Figure 6.15. Fatigue damage in numerical model with the length of unwelded zone 7.2 mm for case 13, (a) $N = 0$ (b) $N = 74,308$ (c) $N = 96,210$ (d) $N = 100,834$

75
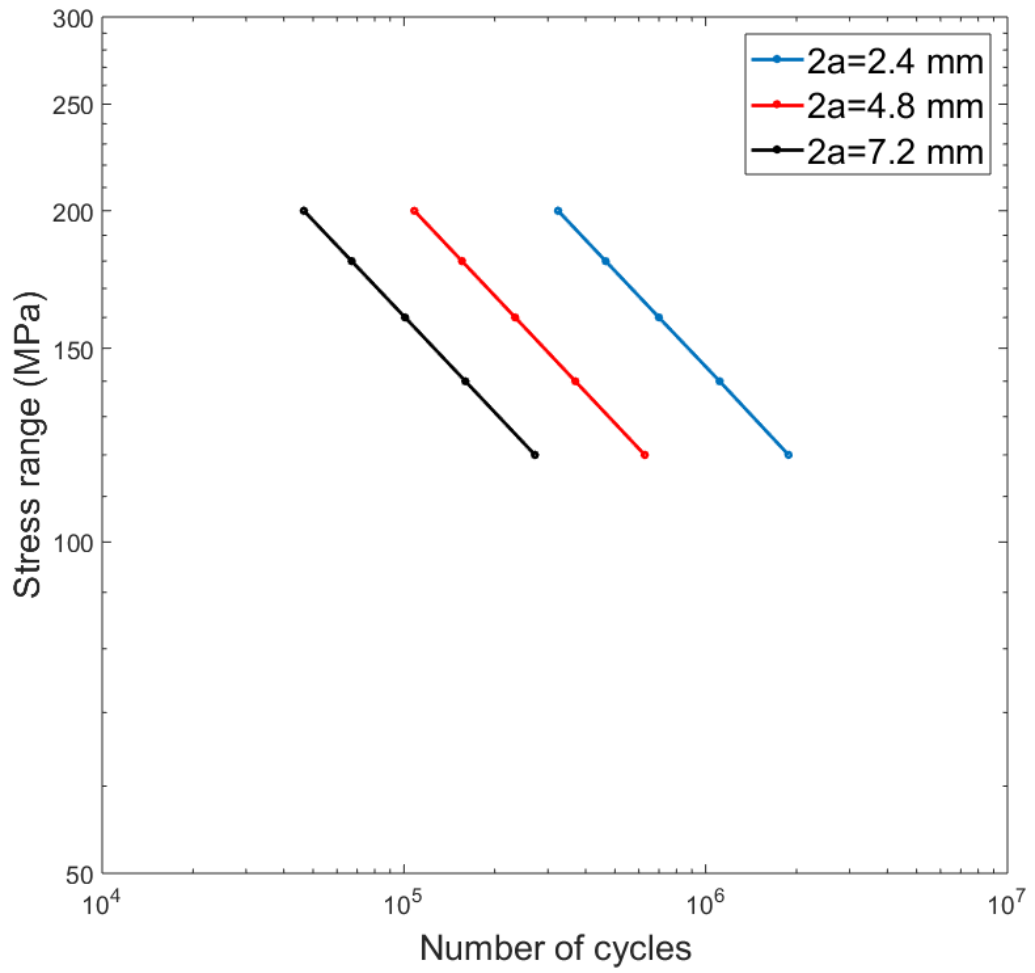
Figure 6.16. Numerical results of fatigue assessment of fillet welded joints
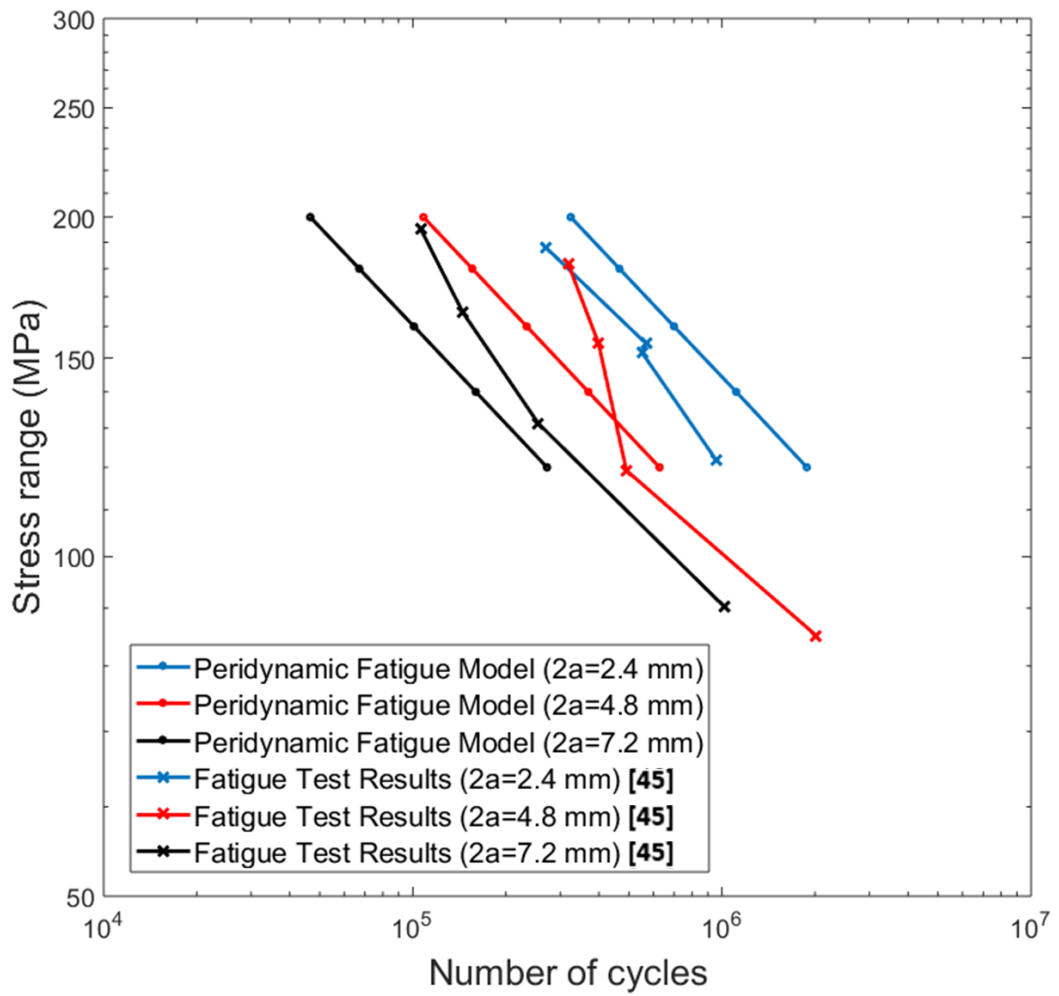
Figure 6.17. Comparison of fatigue performance with fatigue test results of Lee [45]

(a)   (b)
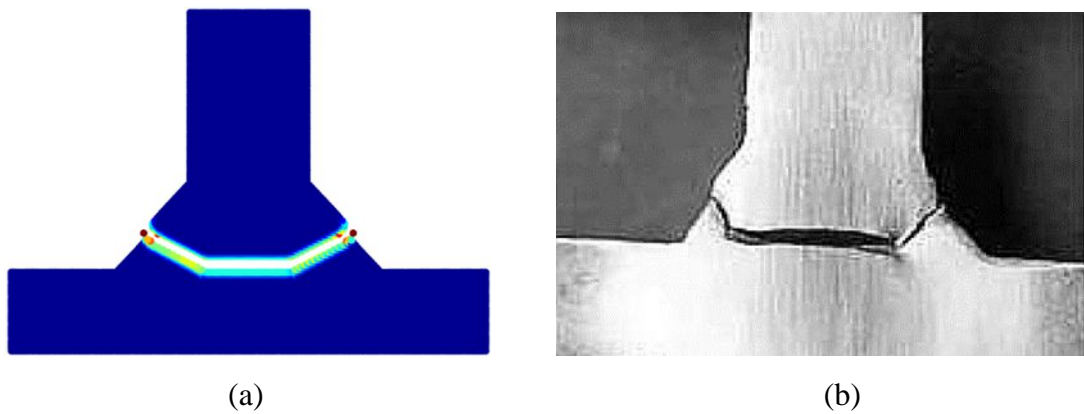
Figure 6.18. Fatigue crack growth path with the length of unwelded zone 7.2 mm, (a) peridynamic fatigue model (b) fatigue test result of Lee [45]

6.5 Conclusion

The fatigue crack growth in fillet welded joints according to the length of unwelded zone is simulated by using the peridynamic fatigue model. The numerical results show that the increase in length of unwelded zone decreases the fatigue performance of fillet welded joints. By comparing the numerical results with the fatigue test results of Lee [45], it is observed that the computational approach with peridynamic fatigue model is capable of estimating the fatigue performance of fillet welded joints. The Fig. 6.17 and 6.18 show that the results of fatigue performance estimated by peridynamic simulations is agreed very well with the fatigue results of Lee [45]. Both results show that increasing the length of unwelded zone deteriorates the fatigue performance of fillet welded joints. In addition, the simulation results of fatigue crack growth path in fillet welded joints are matched very well with the experimental results [45]. The crack is initiated at the pre-existing root crack of unwelded zone and is propagated to both end of weld material sides. Overall, it is confirmed that the peridynamic fatigue model can be used to simulate the actual behaviour of fatigue crack growth for welded joints.

7. CONCLUSION

7.1 Achievements against the objectives

The main objective of this study is to simulate the fatigue crack growth with the peridynamic fatigue model in fillet welded joints and to estimate the fatigue performance by considering the weld geometry effect of the unwelded zone. Achievements of this study are described as below

- The peridynamic fatigue model proposed by Silling and Askari [13] in the crack nucleation phase is validated by numerical fatigue tensile tests with two-dimensional dog-bone shaped specimens under uniaxial tension-compression loadings. The results of peridynamic fatigue model are compared with the fatigue test results of Zhao and Jiang [38]. It is confirmed that the peridynamic fatigue model is capable of predicting the fatigue crack nucleation.

- The peridynamic fatigue model proposed by Silling and Askari [13] in the crack nucleation phase is validated by numerical compact tests with two-dimensional ASTM E647 standard compact specimens under the tension loading. The results of peridynamic fatigue model are compared with the fatigue test results of Zhao and Jiang [40]. This numerical result shows that the peridynamic fatigue model is capable of predicting the fatigue crack growth.

- The fatigue crack growth in fillet welded joints according to the length of unwelded zone is simulated with the peridynamic fatigue model. The numerical results show that the increase in length of unwelded zone in fillet welded joints decreases the fatigue performance. Also, by comparing the numerical results with the fatigue test results of Lee [45], it is confirmed that the computational approach with peridynamic fatigue model is capable of estimating the fatigue performance of fillet welded joints.

7.2 Recommendation for Future studies

There are few future studies as below

- In this study, all material behaviours in peridynamic calculations are assumed as the linear elastic material behaviour. It makes significant errors for ductile materials, which the material behaviour near the crack tip is generally involving the nonlinear plastic material behaviour. It is expected that considering the nonlinear plastic material behaviour in peridynamic calculations can improve prediction capability of simulations.

- The peridynamic fatigue model can be applied to other types of welded joints, and more complicated structure, which the three-dimensional peridynamic model can treat more various types of crack growth. Not only the longitudinal root crack but also other types of crack, such as toe crack, transverse crack, underbead crack, are possible to be simulated.

REFERENCES

1. Teng, T. L., Fung, C. P., & Chang, P. H. (2002). Effect of weld geometry and residual stresses on fatigue in butt-welded joints. International journal of pressure vessels and piping, 79(7), 467-482.

2. Sonsino, C. M. (2009). Effect of residual stresses on the fatigue behaviour of welded joints depending on loading conditions and weld geometry. International Journal of Fatigue, 31(1), 88-101.

3. Barsoum, Z., & Jonsson, B. (2011). Influence of weld quality on the fatigue strength in seam welds. Engineering Failure Analysis, 18(3), 971-979.

4. Ortiz, M., & Pandolfi, A. (1999). Finite-deformation irreversible cohesive elements for three-dimensional crack-propagation analysis. International journal for numerical methods in engineering, 44(9), 1267-1282.

5. Nguyen, O., Repetto, E. A., Ortiz, M., & Radovitzky, R. A. (2001). A cohesive model of fatigue crack growth. International Journal of Fracture, 110(4), 351-369.

6. Moës, N., Gravouil, A., & Belytschko, T. (2002). Non-planar 3D crack growth by the extended finite element and level sets—Part I: Mechanical model. International Journal for Numerical Methods in Engineering, 53(11), 2549-2568.

7. Gravouil, A., Moës, N., & Belytschko, T. (2002). Non-planar 3D crack growth by the extended finite element and level sets—Part II: Level set update. International Journal for Numerical Methods in Engineering, 53(11), 2569-2586.

8. Zi, G., & Belytschko, T. (2003). New crack-tip elements for XFEM and applications to cohesive cracks. International Journal for Numerical Methods in Engineering, 57(15), 2221-2240.

9. Silling, S. A., & Askari, E. (2005). A meshfree method based on the peridynamic model of solid mechanics. Computers & structures, 83(17-18), 1526-1535.

10. Kilic, B., Agwai, A., & Madenci, E. (2009). Peridynamic theory for progressive damage prediction in center-cracked composite laminates. Composite Structures, 90(2), 141-151.

11. Silling, S. A., Weckner, O., Askari, E., & Bobaru, F. (2010). Crack nucleation in a peridynamic solid. International Journal of Fracture, 162(1-2), 219-227.

12. Ha, Y. D., & Bobaru, F. (2010). Studies of dynamic crack propagation and crack branching with peridynamics. International Journal of Fracture, 162(1-2), 229-244.

13. Silling, S. A., & Askari, A. (2014). Peridynamic model for fatigue cracking. SAND2014-18590. Albuquerque: Sandia National Laboratories.

14. Macdonald, K. A., & Maddox, S. J. (2003). New guidance for fatigue design of pipeline girth welds. Engineering Failure Analysis, 10(2), 177-197.

15. Hobbacher, A. (2009). Recommendations for fatigue design of welded joints and components. New York: Welding Research Council.

16. Anderson, T. L. (2017). Fracture mechanics: fundamentals and applications. CRC press.

17. Paris, P., & Erdogan, F. (1963). A critical analysis of crack propagation laws. Journal of basic engineering, 85(4), 528-533.

18. Ferreira, J. M., & Branco, C. M. (1989). Influence of the radius of curvature at the weld toe in the fatigue strength of fillet welded joints. International journal of fatigue, 11(1), 29-36.

19. Nguyen, T. N., & Wahab, M. A. (1995). A theoretical study of the effect of weld geometry parameters on fatigue crack propagation life. Engineering Fracture Mechanics, 51(1), 1-18.

20. Lee, C. H., Chang, K. H., Jang, G. C., & Lee, C. Y. (2009). Effect of weld geometry on the fatigue life of non-load-carrying fillet welded cruciform joints. Engineering Failure Analysis, 16(3), 849-855.

21. Wahab, M. A., & Alam, M. S. (2004). The significance of weld imperfections and surface peening on fatigue crack propagation life of butt-welded joints. Journal of Materials Processing Technology, 153, 931-937.

22. Ninh, N. T., & Wahab, M. A. (1995). The effect of residual stresses and weld geometry on the improvement of fatigue life. Journal of materials processing technology, 48(1-4), 581-588.

23. Teng, T. L., & Chang, P. H. (2004). Effect of residual stresses on fatigue crack initiation life for butt-welded joints. Journal of Materials Processing Technology, 145(3), 325-335.

24. Magudeeswaran, G., Balasubramanian, V., Reddy, G. M., & Balasubramanian, T. S. (2008). Effect of welding processes and consumables on tensile and impact properties of high strength quenched and tempered steel joints. Journal of iron and steel research, international, 15(6), 87-94.

25. Hillerborg, A., Modéer, M., & Petersson, P. E. (1976). Analysis of crack formation and crack growth in concrete by means of fracture mechanics and finite elements. Cement and concrete research, 6(6), 773-781.

26. De-Andrés, A., Pérez, J. L., & Ortiz, M. (1999). Elastoplastic finite element analysis of three-dimensional fatigue crack growth in aluminum shafts

subjected to axial loading. International Journal of Solids and Structures, 36(15), 2231-2258.

27. Nguyen, O., Repetto, E. A., Ortiz, M., & Radovitzky, R. A. (2001). A cohesive model of fatigue crack growth. International Journal of Fracture, 110(4), 351-369.

28. Belytschko, T., & Black, T. (1999). Elastic crack growth in finite elements with minimal remeshing. International journal for numerical methods in engineering, 45(5), 601-620.

29. Moës, N., Gravouil, A., & Belytschko, T. (2002). Non-planar 3D crack growth by the extended finite element and level sets—Part I: Mechanical model. International Journal for Numerical Methods in Engineering, 53(11), 2549-2568.

30. Gravouil, A., Moës, N., & Belytschko, T. (2002). Non-planar 3D crack growth by the extended finite element and level sets—Part II: Level set update. International Journal for Numerical Methods in Engineering, 53(11), 2569-2586.

31. Sukumar, N., Chopp, D. L., & Moran, B. (2003). Extended finite element method and fast marching method for three-dimensional fatigue crack propagation. Engineering Fracture Mechanics, 70(1), 29-48.

32. Silling, S. A. (2000). Reformulation of elasticity theory for discontinuities and long-range forces. Journal of the Mechanics and Physics of Solids, 48(1), 175-209.

33. Madenci, E., & Oterkus, E. (2016). Peridynamic theory and its applications. Springer.

34. Oterkus, E., Guven, I., & Madenci, E. (2010, June). Fatigue failure model with peridynamic theory. In Thermal and Thermomechanical Phenomena in Electronic Systems (ITherm), 2010 12th IEEE Intersociety Conference on (pp. 1-6). IEEE.

35. Kilic, B., & Madenci, E. (2010). An adaptive dynamic relaxation method for quasi-static simulations using the peridynamic theory. Theoretical and Applied Fracture Mechanics, 53(3), 194-204.

36. Cagan. Diyaroglu, (2016). Peridynamics and its applications in marine structures. Thesis [Ph. D] -- University of Strathclyde, 2016, Thesis no.: T14264.

37. Silling, S. A. (2010). Linearized theory of peridynamic states. Journal of Elasticity, 99(1), 85-111.

38. Zhao, T., & Jiang, Y. (2008). Fatigue of 7075-T651 aluminum alloy. International Journal of Fatigue, 30(5), 834-849.

39. Zaccariotto, M., Luongo, F., & Galvanetto, U. (2015). Examples of applications of the peridynamic theory to the solution of static equilibrium problems. The Aeronautical Journal, 119(1216), 677-700.

40. Zhao, T., Zhang, J., & Jiang, Y. (2008). A study of fatigue crack growth of 7075-T651 aluminum alloy. International Journal of Fatigue, 30(7), 1169-1180.

41. Kujawski, D. (2001). A fatigue crack driving force parameter with load ratio effects. International Journal of Fatigue, 23, 239-246.

42. Shim, J. S., Kim, C. H., & Kim, D. J. (2004). 3D Finite Element Analysis of High Tension Bolted Joints. Journal of Korean society of steel construction, Korean society of steel construction, 16(4), 407-413.

43. DeMarte, R. A. (2016). Analysis of Fatigue Crack Propagation in Welded Steels.

44. Oterkus, S., Madenci, E., & Agwai, A. (2014). Peridynamic thermal diffusion. Journal of Computational Physics, 265, 71-96.

45. Lee, Y. B. (2010). Characteristics of Fatigue Failure according to Thickness of Material and Number of Passes in Cruciform Fillet Weld Zone. Journal of Welding and Joining, 28(6), 45-50.